Learned Compressive Representations for Single-Photon 3D Imaging

Felipe Gutierrez-Barragan[1‡], Fangzhou Mu[1], Andrei Ardelean[3], Atul Ingle[2], Claudio Bruschini[3], Edoardo Charbon[3], Yin Li[1], Mohit Gupta[1], Andreas Velten[1]
[1]University of Wisconsin-Madison, [2]Portland State University,
[3]Ecole Polytechnique Federale de Lausanne

Abstract

Single-photon 3D cameras can record the time-of-arrival of billions of photons per second with picosecond accuracy. One common approach to summarize the photon data stream is to build a per-pixel timestamp histogram, resulting in a 3D histogram tensor that encodes distances along the time axis. As the spatio-temporal resolution of the histogram tensor increases, the in-pixel memory requirements and output data rates can quickly become impractical. To overcome this limitation, we propose a family of linear compressive representations of histogram tensors that can be computed efficiently, in an online fashion, as a matrix operation. We design practical lightweight compressive representations that are amenable to an in-pixel implementation and consider the spatio-temporal information of each timestamp. Furthermore, we implement our proposed framework as the first layer of a neural network, which enables the joint end-to-end optimization of the compressive representations and a downstream SPAD data processing model. We find that a well-designed compressive representation can reduce in-sensor memory and data rates up to 2 orders of magnitude without significantly reducing 3D imaging quality. Finally, we analyze the power consumption implications through an on-chip implementation.

1. Introduction

3D cameras based on single-photon avalanche diode technology (SPAD) are becoming increasingly popular for a wide range of applications that require high-resolution and low-power depth sensing, ranging from autonomous vehicles [1] to consumer smartphones [2]. Kilo-to-megapixel resolution SPAD pixel arrays [30, 31] have the capability of capturing the time-of-arrival of billions of individual photons per frame with extremely high (picosecond) time resolution [35]. Unfortunately, this extreme sensitivity and high speed comes at a cost — the raw timestamp data causes a severe bottleneck between the image sensor and the image signal processor (ISP) that processes this data (Fig. 1(a)). This data bottleneck severely limits the wider use of high-resolution SPAD arrays in 3D sensing applications.

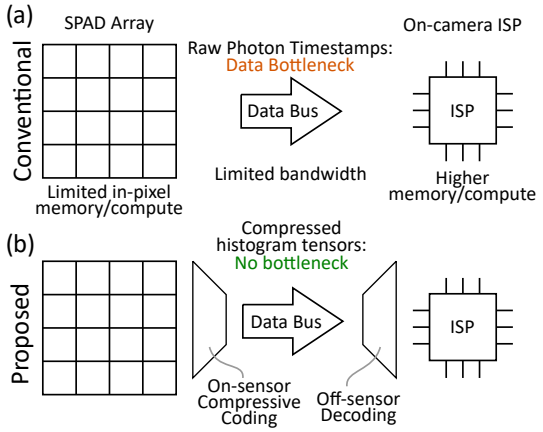

Figure 1. **Resolving SPAD data bottleneck with learned compression.** (a) Conventional SPAD-based 3D cameras stream raw photon timestamps or summary histograms off the image sensor which causes a data bottleneck between the image sensor and the on-camera image and signal processing (ISP) module. (b) Our method applies a lightweight, on-sensor compressive coding scheme to the photon timestamp data which is later decoded at the ISP, resolving the data bandwidth limitation.

One common approach to avoid transferring individual photon timestamps is to build a histogram in each pixel. This results in a 3D histogram tensor that is transferred off-sensor for processing. Although this may be practical at low spatio-temporal resolutions (e.g., 64x32 pixels with 16 time bins [18]), it requires higher in-sensor memory. Moreover, the data rates of this histogram tensor representation also scale rapidly with the spatio-temporal resolution and maximum depth range. For example, a megapixel SPAD-based 3D camera operating at 30 fps that outputs a histogram tensor with a thousand 8-bit bins per pixel would require an unmanageable data transfer rate of 240 Gbps.

To overcome the above limitations, we seek to design compressive representations of 3D histogram tensors. In order to reduce the data rates output by the SPAD camera, the compact representation needs to be built in-pixel or inside the focal plane array (FPA). This is illustrated in Fig. 1(b). Due to the limited in-pixel memory and compute, the compressive representation needs to be built in a streaming manner, with minimal computations per photon. Photon

‡Email: fgutierrez3@wisc.edu

histogram tensors are very different from conventional RGB images/video data. Therefore, traditional compression algorithms such as MPEG are not directly applicable.

We propose a family of compressive representations for 3D histogram tensors that can be computed in an online fashion with limited memory and compute. They are based on the *linear spatio-temporal projection* of each photon timestamp, which can be expressed as a simple matrix operation. Instead of constructing per-pixel timestamp histograms, a compressive encoding maps its spatio-temporal information into a *compressive histogram*. To exploit local spatio-temporal correlations, a single compressive histogram is built for a local 3D histogram block as illustrated in Fig. 2. Instead of building and storing the full 3D histogram tensor in-sensor, multiple compressive histograms are built and transferred off-sensor for processing, effectively reducing the required in-sensor memory and data rates. Recent works proposed a similar compression framework based on compressive histograms [16] or sketches [40]. In Sec. 4, we show that these prior works can be viewed as special cases of our proposed framework.

In this paper, we explore the design space of spatio-temporal compressive encodings and analyze the trade-offs between different design choices. Furthermore, we present a method to integrate our compression framework with data-driven SPAD data processing methods using convolutional neural networks (CNNs), which enables end-to-end optimization of the compressive encoding and a SPAD data processing CNN. We demonstrate the feasibility of compressive histograms through an on-chip implementation.

For our experimental evaluation, we integrate the compressive histograms framework with a state-of-the-art learning-based denoising model for SPAD-based 3D imaging [36]. Our results show that the jointly optimized compressive encoding and CNN can consistently reduce data rates up to 2 orders of magnitude in a wide range of signal and noise levels. Moreover, for a given compression level, it can increase 3D imaging accuracy over previous hand-designed compressive histograms that only exploit temporal information [16, 40], especially in low signal-to-background ratio (SBR) scenarios and at higher compression rates. Furthermore, we show that learned compressive histograms can perform comparably and sometimes even outperform a theoretical SPAD sensor design where the full 3D histogram tensor is stored in-sensor and only per-pixel depths are transferred off-sensor. Finally, we analyze the power consumption of a compressive histogram implemented on the UltraPhase SPAD processing chip [4].

2. Related Work

Compressive histograms, also called sketches, are an emerging framework for online in-sensor compression of SPAD timestamp data [16, 45, 40, 37]. A coarse histogram is one common compressive histogram approach [16] to reduce data rates and in-pixel memory [18, 10, 21]. Despite their practical hardware implementation, coarse histograms achieve sub-optimal depth accuracy compared to compressive histograms based on Fourier [40, 41, 16] and Gray [16] codes. One limitation of these approaches is that the compressive representation only exploits the temporal information of the incident timestamp, and disregards the spatial redundancy. In this work, we generalize the compressive histogram framework to utilize the *spatio-temporal information of each timestamp*. Moreover, instead of relying on hand-designed coded projections, in this paper we learn them as the first layer of a CNN.

Shared In-Pixel Histograms: One common design is to have multiple neighboring SPAD pixels have a single shared memory where all timestamps are aggregated into a coarse histogram (e.g., 4×4 [21, 18], 3×3 [23]). This approach throws away the local spatial information (i.e., pixel location) of the detected photon timestamps. A compressive histogram is well-suited for these shared memory designs because it can be shared among multiple SPAD pixels and preserves spatial information through the coded projection.

Neural Sensors and Pixel Processor Arrays: Pixel processor arrays (PPAs) are an emerging sensing technology that embeds processing electronics inside each pixel [11]. This new sensing paradigm begins processing the image at the focal plane array, which allows it to reduce the sensor data rates by transmitting only the relevant information, and consequently, it increases the sensor's throughput [11] which can enable computer vision at 3,000 fps [6, 7]. PPAs have also become building blocks of novel computational imaging systems optimized end-to-end for HDR imaging [28, 43], motion deblurring [33], video compressive sensing [28], and light field imaging [47]. A compressive histogram relies on a similar *in-pixel processing* paradigm. Similar to previous works, we jointly optimize the sensor parameters (i.e., the compressive histogram) and the processing algorithm (i.e., the CNN), but to our knowledge, this work is the first to use this approach for SPAD data compression.

3. Single-Photon 3D Histogram Tensors

SPAD-based 3D cameras consist of a SPAD sensor and a pulsed laser that illuminates the scene. The photon flux signal arriving at pixel, $\boldsymbol{p}$, can be written as:

$$\Phi_{\boldsymbol{p}}(t) = a_{\boldsymbol{p}} h(t - 2d_{\boldsymbol{p}}/c) + \Phi_{\boldsymbol{p}}^{\text{bkg}} = \Phi_{\boldsymbol{p}}^{\text{sig}}(t) + \Phi_{\boldsymbol{p}}^{\text{bkg}}, \quad (1)$$

where $a_{\boldsymbol{p}}$ is the amplitude of the returning signal accounting for laser power, reflectivity, and light fall-off; $h(t)$ is the system's impulse response function (IRF) which accounts for pulse waveform and sensor IRF; $d_{\boldsymbol{p}}$ is the distance to the point imaged by $\boldsymbol{p}$; c is the speed of light; and $\Phi_{\boldsymbol{p}}^{\text{bkg}}$ is the constant photon flux due to background illumination (e.g., sunlight). This model assumes direct-only reflections

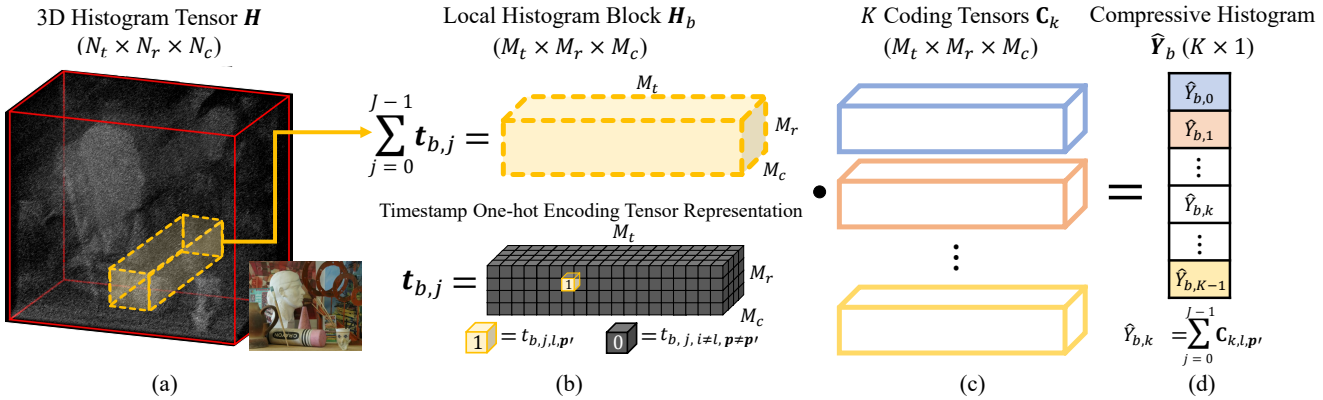

Figure 2. **Compressive Histogram Formation.** Histogram tensors, $\boldsymbol{H}$, are a 3D spatio-temporal grid whose elements store the number of photons that arrived within a short time interval. (a) In SPAD-based 3D imaging, the temporal axis of $\boldsymbol{H}$ encodes distances. (b) A histogram block, $\boldsymbol{H}_b$, can be expressed as the sum of J one-hot encoding tensors, where each tensor represents a photon timestamp. (c) A compact representation of $\boldsymbol{H}_b$ can be built by applying K linear projections (i.e., dot product) with pre-designed coding tensors. (d) The compressive histogram, will be a vector with K elements whose compression capacity is given by $\frac{M_t \cdot M_r \cdot M_c}{K}$.

which is a valid approximation, in particular, for scanning-based ToF 3D imaging systems [3].

TCSPC-based SPAD cameras measure $\Phi_{\boldsymbol{p}}(t)$ by building a per-pixel timing histogram, where the ith histogram bin records the number of photons that arrived in a time interval of length Δ, which follows a Poisson process $\mathcal{P}$:

$$\Phi_{i,\boldsymbol{p}} = \mathcal{P}(\Phi^{\text{sig}}_{i,\boldsymbol{p}} + \Delta\Phi^{\text{bkg}}_{\boldsymbol{p}}). \tag{2}$$

The pulse repetition period, τ, determines the maximum timestamp value and the length of the histogram vector $\boldsymbol{\Phi}_{\boldsymbol{p}} = (\Phi_{i,\boldsymbol{p}})_{i=0}^{N_t-1}$, where $N_t = \tau/\Delta$. Therefore, one assumption built into $\boldsymbol{\Phi}_{\boldsymbol{p}}$, is that no signal photons had a timestamp larger than τ, which means that the maximum distance that $\boldsymbol{\Phi}_{\boldsymbol{p}}$ can encode is $d_{\text{max}} = \frac{c\tau}{2}$. Furthermore, we assume that pile-up distortions are minimized through various SPAD data acquisition techniques [13, 18, 19, 14].

This process generates a $N_t \times N_r \times N_c$ 3D histogram tensor, $\boldsymbol{H} = (\boldsymbol{\Phi}_{\boldsymbol{p}})_{\boldsymbol{p}=(0,0)}^{(N_r-1,N_c-1)}$. In challenging 3D imaging scenarios with high background illumination, building $\boldsymbol{H}$ off-sensor requires transferring thousands of photon timestamps per-pixel leading to data rates of hundreds of GB/s in a megapixel sensor. Moreover, building and storing a high-resolution $\boldsymbol{H}$ in-sensor would require significant memory (1GB for a megapixel SPAD camera with 1000 time bins per-pixel), and transferring it would continue to lead to impractical data rates of tens of GB/s on a SPAD-based 3D camera operating at 30fps. Overall, a practical SPAD-based 3D camera would build and store a *compact representation* of $\boldsymbol{H}$ in-sensor and then transfer it to a processing chip (e.g., FPGA, ISP, embedded computer) where it is processed.

4. Spatio-temporal Compressive Histograms

A natural approach to compress $\boldsymbol{H}$ that exploits its local correlations due to smooth depths and photon flux, is to build a compressive representation of a local 3D histogram block as illustrated in Fig. 2. To avoid storing or transferring the photon timestamp stream, the compressive representation is built as each timestamp arrives. In this section, we present an online compression framework for histogram blocks based on the coded projection of photon timestamps.

Let $\boldsymbol{H}_b$ be the bth histogram block of $\boldsymbol{H}$ with dimensions $M_t \times M_r \times M_c$, where $M_t \leq N_t$, $M_r \leq N_c$, and $M_c \leq N_c$. First, we observe that $\boldsymbol{H}_b$ can be expressed as the sum of J one-hot encoding tensors, each representing one photon detection within $\boldsymbol{H}_b$ (Fig. 2b). Specifically, let $\boldsymbol{t}_{b,j}$ be a $M_t \times M_r \times M_c$ one-hot encoding tensor representing the j^{th} photon timestamp detected in histogram block $\boldsymbol{H}_b$, whose elements are all 0 except for $t_{b,j,l,\boldsymbol{p}'} = 1$, where $l = \lfloor \frac{T_j \mod (\Delta M_t)}{\Delta} \rfloor$, T_j is the timestamp value, and $\boldsymbol{p}'$ is the pixel where the timestamps was detected. Using this representation we can write $\boldsymbol{H}_b$ as follows:

$$\boldsymbol{H}_b = \sum_{j=0}^{J-1} \boldsymbol{t}_{b,j}\ . \tag{3}$$

$\boldsymbol{H}_b$ can be compressed in an online fashion through the linear projection of each timestamp tensor; expressed as the inner product with K pre-designed *coding tensors*, $\mathbf{C}_k$, with dimensions $M_t \times M_r \times M_c$, as in Fig. 2. Mathematically,

$$\widehat{Y}_{b,k} = \mathbf{C}_k \cdot \boldsymbol{H}_b = \sum_{j=0}^{J-1} \mathbf{C}_k \cdot \boldsymbol{t}_{b,j} = \sum_{j=0}^{J-1} \mathbf{C}_{k,l,\boldsymbol{p}'}, \tag{4}$$

where $\cdot$ denotes element-wise multiplication, and l and $\boldsymbol{p}'$ are the indices where $\boldsymbol{t}_{b,j,l,\boldsymbol{p}'} = 1$. We define $\widehat{\boldsymbol{Y}}_b = (\widehat{Y}_{b,k})_{k=0}^{K-1}$ as the *compressive histogram* of $\boldsymbol{H}_b$. Compressive histograms, as defined in [16, 40], are a special case of Eq. 4 where $\mathbf{C}$ compresses individual histograms and disregards spatial information (i.e., M_t=N_t, M_r=1, M_c=1) Note that each timestamp in Eq. 4 is processed efficiently on-the-fly after each photon detection through a simple lookup

operation. Moreover, individual histogram blocks or timestamps are never explicitly stored or transferred off-sensor.

4.1. Practical Coding Tensor Design

Compressive histograms, when implemented as in Eq. 4, introduce an in-sensor memory overhead because, in addition to storing $\widehat{\boldsymbol{Y}}_b$, $\mathbf{C}$ needs to be stored in-sensor for efficient lookup operations. Therefore, a practical compressive single-photon camera implementation would rely on parameter-efficient coding tensors that minimize this overhead. Here, we present two strategies to design practical coding tensors that are evaluated in Sec. 6.

The memory overhead makes certain coding tensor designs impractical. Consider a set of coding tensors that operate on the full histogram tensor, i.e., $\boldsymbol{H}_b = \boldsymbol{H}$.In this case, the number of elements in $\mathbf{C}$ will exceed the number of elements of $\boldsymbol{H}$. Consequently, although the data rates are reduced in this scenario since $K < (N_t \cdot N_r \cdot N_c)$, the in-sensor memory required exceeds the size of the histogram tensor. To circumvent this issue, we propose two complementary strategies to design lightweight coding tensors: local block-based and separable.

Local Block-based Coding Tensors: As we reduce the size of the histogram block, $\boldsymbol{H}_b$, represented by a compressive histogram, the size of the coding tensors decreases. Therefore, compressing local histogram blocks is not only beneficial due to local spatio-temporal redundancies, but also because these local coding tensors have fewer parameters. One example of local block-based coding tensors are the ones used in temporal compressive histograms [16, 40] where $\boldsymbol{H}_b$ is a per-pixel histogram.

Separable Coding Tensors: One approach to designing lightweight coding tensors is to make them separable along the temporal and spatial dimensions. This approach is used in parameter-efficient CNN models that use separable depth-wise convolutional layers [20] to reduce model size. Formally, we can write a separable coding tensor as the outer product of two smaller tensors:

$$\mathbf{C}_k = \mathbf{C}_k^{\text{temporal}} \otimes \mathbf{C}_k^{\text{spatial}}, \tag{5}$$

where $\mathbf{C}_k^{\text{temporal}}$ is a $M_t \times 1 \times 1$ tensor, and $\mathbf{C}_k^{\text{spatial}}$ is a $1 \times M_r \times M_c$ tensor. This design is also motivated by the differences between the temporal and spatial correlations encountered in histogram blocks. In addition to local correlations present in both dimensions, the temporal dimension also exhibits long-range correlations due to the background illumination offset ($\Phi_{\boldsymbol{p}}^{\text{bkg}}$) in every histogram bin. Therefore, Eq. 5 may be able to represent this prior by encoding the temporal and spatial information independently.

One assumption made in our memory overhead analysis is that a compressive SPAD-based 3D camera only needs to store a single $\mathbf{C}$ that is shared across the full sensor, which can be implemented in two general ways. One approach could distribute $\mathbf{C}$ across the local memory of all pixels and then allow communication across pixels as in PPAs [6]. A second approach could store $\mathbf{C}$ in a global memory that can be accessed by all pixels which could be enabled in 3D-stacked SPAD cameras [49]. Finally, some of the coding tensor designs explored in this paper have as few as 640 parameters. In this case, even if $\mathbf{C}$ is stored for every 4×4 group of pixels, the in-sensor memory is still reduced by $20\times$ compared to storing a 1024 bin per-pixel histogram.

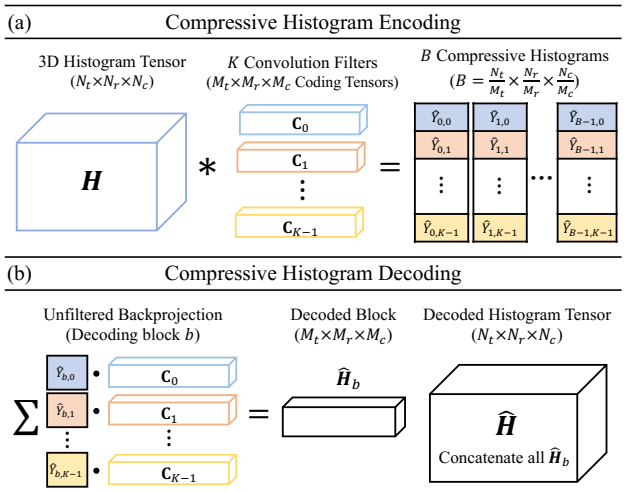

Figure 3. **Convolutional Compressive Histogram Layer.** (a) Building a compressive histogram for each block in the histogram tensor, can be viewed as applying K strided convolutional filters whose weights are the coding tensors. The compressed histogram tensor will be K $\frac{N_t}{M_t} \times \frac{N_r}{M_r} \times \frac{N_c}{M_c}$ tensors. (b) To lift the compressed histogram tensor back to its original domain an unfiltered backprojection operation can be applied on each compressive histogram which decodes a single block. The decoded histogram tensor can then be assembled by concatenating all the decoded blocks.

4.2. Convolutional Compressive Histogram Layer

A compressive histogram is built for each histogram block. Therefore, multiple compressive histograms are used to encode the complete histogram tensor. In this way, the coding tensors can be viewed as a set of 3D convolutional filters, which can be implemented as the first layer of a 3D CNN. For simplicity, we assume that histogram blocks do not overlap, and therefore, the stride of the convolutional filters will equal their dimensions. Fig. 3(a) illustrates this convolutional compressive histogram encoding.

Unfortunately, the compressed histogram tensor representation is not directly compatible with 3D CNNs that have been designed for SPAD-based 3D imaging (e.g., [36, 24]). To this end, each compressive histogram is lifted back to the original 3D domain through an unfiltered backprojection:

$$\widehat{\boldsymbol{H}}_b = \sum_{k=0}^{K-1} \mathbf{C}_k \widehat{Y}_{b,k} \; . \tag{6}$$

Here $\widehat{\boldsymbol{H}}_b$ is the decoded compressive histogram for block b, which is the weighted linear combination of the coding tensors. The decoded histogram blocks are then concatenated and given as input to the processing 3D CNN. Fig. 3(b) illustrates this decoding step. The decoding step in Eq. 6 will occur off-sensor, after the compressive histograms have been moved to the camera compute module which has access to larger memory and computational resources than sensor module. One benefit of using the unfiltered backprojection as the upsampling operator is that if all coding tensors are mutually orthogonal, in the limit when K approaches the size of $\boldsymbol{H}_b$ (i.e., no compression), then $\widehat{\boldsymbol{H}}_b \approx \boldsymbol{H}_b$. This suggests that at compresion rates close to unity, an appropriately trained compressive histogram layer should be approximately equal to an identity transformation applied to $\boldsymbol{H}_b$.

To summarize, a compressive histogram layer comprises an encoding/compression step followed by a decoding step, which uses the coding tensors as the convolutional filters. This layer can be appended to the beginning of any CNN that has been designed to process 3D histogram tensors. Finally, the coding tensors can be jointly optimized with the downstream CNN in an end-to-end manner.

5. Datasets and Implementation

In this section, we describe the datasets used for model training and testing, and also provide implementation details for the compressive histogram layer and the 3D CNN used for the experiments.

5.1. Datasets

For training, we generate a synthetic SPAD measurement dataset containing different scenes at a wide range of illumination settings. We use a similar synthetic data generation pipeline used in previous learning-based SPAD-based 3D imaging works [24, 36, 44]. Using Eq. 2, SPAD measurements can be simulated given an RGB-D image, the pulse waveform ($h(t)$), and the average number of detected signal and background photons per pixel. Please refer to the supplement for a detailed overview of the simulation pipeline.

Simulated Training Dataset: We use the RGB-D images from the NYU v2 dataset [42]. The simulated histograms have $N_t = 1024$ bins and a $\Delta = 80$ps bin size (12.3m depth range). The pulse waveform used has a full-width half maximum (FWHM) of 400ps obtained from [24]. For each scene, we randomly set the average number of signal and background photons detected per pixel to [2, 5, or 10] and [2, 10, 50], respectively. With appropriate normalization, the models generalize to other photon levels despite being trained on this photon-starved dataset. A total of 16,628 histogram tensors with dimensions $1024 \times 64 \times 64$ are simulated and split into a training and a validation set with 13,851 and 2,777 examples, respectively.

Simulated Test Dataset: For testing we use 8 RGB-D images from the Middlebury stereo dataset [39]. The simulated histograms have $N_t = 1024$ bins and a $\Delta = 100$ps bin size (15.3m depth range). The pulse waveform used is a Gaussian pulse with an FWHM of 318ps ($\sigma = 135$ps). A total of 128 test histogram tensors are generated by simulating each scene with the following average number of detected signal/background photons: 2/2, 2/5, 2/50, 5/2, 5/10, 5/50, 10/2, 10/10, 10/50, 10/200, 10/500, 10/1000, 50/50, 50/200, 50/500, and 50/1000.

Real-world Experimental Data: To evaluate the generalization of the proposed models, we downloaded raw histogram tensor captured in [24] with a line-scanning SPAD-based 3D camera prototype. Please refer to the supplementary document for details on this dataset.

5.2. Training and Implementation

To simplify training, the input to all models is a 3D histogram tensor, even though compressive histograms can work directly on streams of photon timestamps (Eq. 4).

Compressive Histogram Layer: The encoder is implemented as a 3D convolution with a stride equal to the filter size, whose learned filters are the coding tensors, $\mathbf{C}_k$. We constraint $\mathbf{C}_k$ to be zero-mean along the time dimension. The unfiltered backprojection decoder is implemented as a 3D transposed convolution with a stride equal to its filter size.To help the CNN model generalize to different photon count levels we apply zero-normalization along the channel dimension (i.e., K) to the inputs ($\widehat{\boldsymbol{Y}}_b$) and the weights ($\mathbf{C}$) of the transposed convolution, also known as layer-norm [5]. This normalization is also commonly used in depth decoding algorithms [17, 16, 29].

Depth Estimation 3D CNN: To estimate depths from the decoded histogram tensor we use the 3D deep boosting CNN model proposed by [36] for single-photon 3D imaging, without the non-local block. Similar to [24, 36] we use the pixel-wise KL-divergence between the output histogram tensor and a normalized true histogram tensor as our objective, and estimate depths using a softargmax.

Training: At each training iteration we randomly sample patches of size $1024 \times 32 \times 32$. We train all models using the ADAM optimizer [22] with $\beta_1 = 0.9$, $\beta_2 = 0.999$, batch size of 4, and a learning rate of 0.001 that decays by 0.9 after every epoch. We train all models for 30 epochs with periodical checkpoints, and for a given model we choose the checkpoint that achieves the lowest root mean squared error (RMSE) on the validation set.

6. Experiments and Results

In this section, we present the performance at various compression levels for different coding tensor designs jointly optimized with the depth estimation CNN described in Sec. 5. A coding tensor design is determined by the

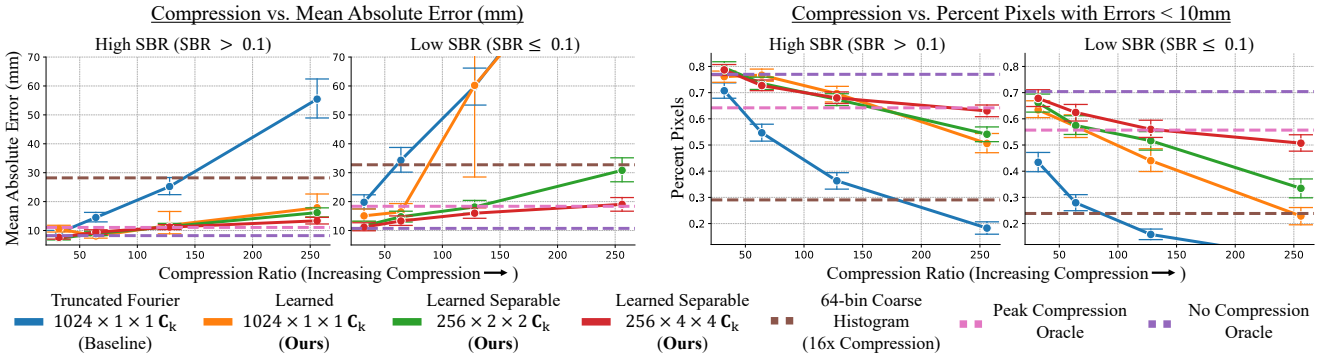

Figure 4. **Compression vs. Test Set Metrics.** The two left-most plots show the mean absolute error computed over the test set as we increase compression. Similarly, the two right-most plots show the mean percent of pixels whose absolute depth errors were < 10mm. The simulated test set images were divided into low (SBR ≤ 0.1) and high (SBR > 0.1) SBR groups to be able to disentangle the impact of SBR on the performance of each model. The dashed lines show the peak and no compression baselines whose compression levels do not vary. Each line corresponds to a fixed coding tensor design for which we vary K to control the compression level. Moreover, each point for a given compression level corresponds to a single set of coding tensors jointly optimized with the depth estimation 3D CNN.

dimensions of $\mathbf{C}_k$ (i.e., $M_t \times M_r \times M_c$), the size of the compressive histogram (i.e., K), and if $\mathbf{C}_k$ is separable.

6.1. Baselines and Performance Metrics

We compare against the following baselines:

- **Temporal Truncated Fourier C [40, 16]:** A compressive histogram that uses coding tensors with dimensions $1024 \times 1 \times 1$ and whose weights are set using the first $K/2$ frequencies of the Fourier matrix. In the supplement, we compare against additional Fourier-based $\mathbf{C}$ [16].
- **Temporal Coarse Histogram C:** Here $\mathbf{C}$ is a box downsampling operator along the temporal dimensions which produces a coarse histogram with K bins.
- **No Compression Oracle:** In this baseline, we assume the ideal scenario where the histogram tensor is transferred off-sensor and processed with the depth estimation 3D CNN. Similar to [36], we train this model with an initial learning rate of 10^{-4} and total variation regularization.
- **Peak Compression Oracle:** This baseline implements an ideal SPAD camera with sufficient in-sensor memory to store the histogram tensor and sufficient computation power to compute per-pixel depths through an "argmax" along the time axis. To process the noisy 2D depth images with the 3D CNN, we generate a 3D grid where all elements are zero except for one element per spatial location whose index is proportional to the depth. This model is trained like the no-compression oracle.

Similar to our proposed approach, all compressive histogram baselines described here, implemented their $\mathbf{C}$ as a compressive histogram layer, with fixed weights, whose outputs are processed by the depth estimation 3D CNN.

Evaluation Metrics: The 3D imaging performance of each model is summarized using two metrics: (1) the mean absolute depth error (MAE), (2) and the percent of pixels with absolute depth errors that are lower than 10mm. To understand the performance under these metrics we divide the test set into different SBR ranges and report the metrics for each range individually. We also visualize the overall dataset performance as scatter plots (e.g., Fig. 7) where each point shows the MAE for a given test scene and their color hue represents the mean SBR of the scene. Outliers with an MAE larger than 50mm are not visible in the plot, however, they are included in the calculation of the statistics. Finally, when comparing different compressive histogram strategies the compression ratio is fixed. The compression ratio (CR) is the ratio of the block size and the length of the compressive histogram (i.e., CR $= (M_t \cdot M_r \cdot M_c \cdot)/K$).

6.2. 3D Imaging Performance

Compression vs. Performance: Fig. 4 shows the performance of compressive histograms as a function of the compression ratio. The learned coding tensors consistently outperform the temporal Fourier-based $\mathbf{C}$. At low SBR and CR > 100, it becomes essential for the learned coding tensors to utilize spatio-temporal information (i.e., green and red lines). Moreover, the proposed models can outperform the peak compression oracle for CR ≤ 64. Overall, learned spatio-temporal coding tensors provide robust performance that degrades gracefully as compression increases.

Importance of Learned Coding Tensors: Fig. 5 compares the depth reconstructions of compressive histograms with coding tensors that were optimized (ours) against coding tensors that were fixed and not optimized throughout training. The extreme quantization in coarse histograms causes large systematic depth errors. Random unoptimized coding tensors consistently produce lower-quality depth reconstructions. A well-designed coding tensor based on Fourier codes can produce reasonable depth reconstructions at 64x compression, however, at 128x compression, scene details become blurred. The proposed learned coding tensors are

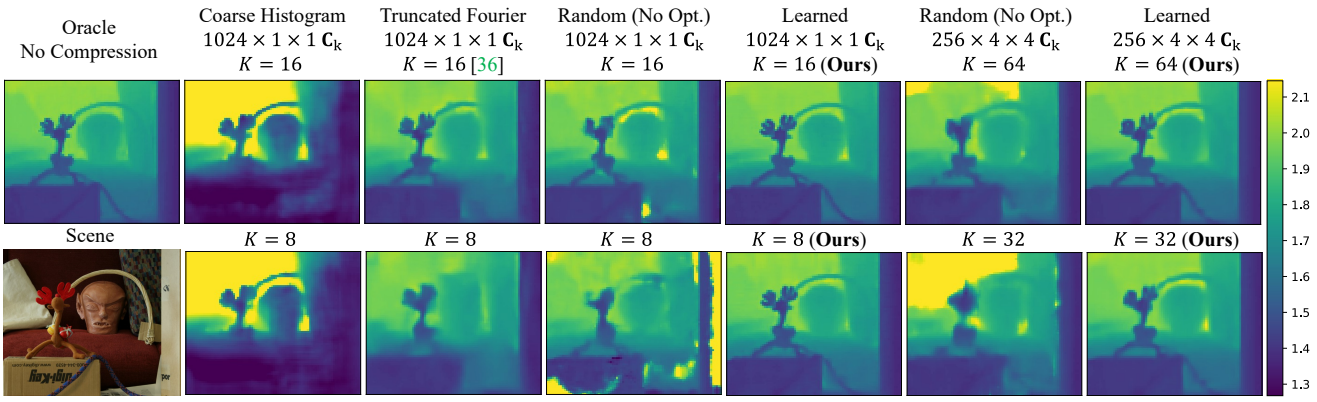

Figure 5. **Importance of Learned Coding Tensors.** Depth reconstructions at 64x (top) and 128x (bottom) compression for compressive histogram models whose coding tensors were hand-designed (coarse histogram and Fourier-based), learned (proposed), and not learned (randomly initialized). The simulated scene had an SBR=0.1, where the mean signal and background photon levels were [50, 500].

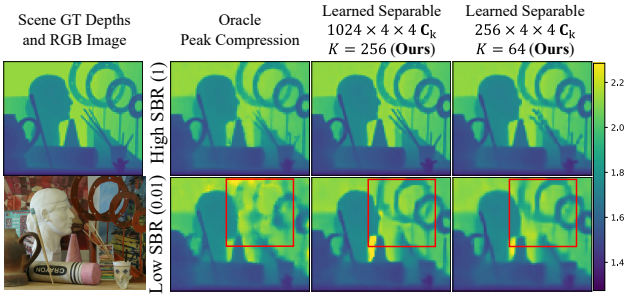

Figure 6. **What if we could compute depths in-pixel?** Depth reconstructions at high and low SBR with mean signal and background photon levels of [10, 10] and [10, 1000], respectively. The compressive histograms have a compression of 64.

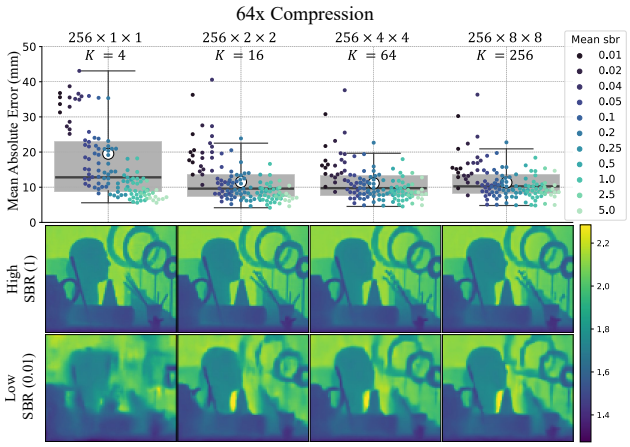

Figure 7. **When do spatio-temporal coding tensors help?** Each scatter plot point corresponds to the MAE of a test scene. The images directly below each model correspond to the depth reconstructions for two test examples at high and low SBR levels whose mean signal and background photons per pixel are [10, 10] and [10, 1000], respectively. For a fixed compression level, the spatial block size of each model is increased from left to right and K is adjusted to maintain the same compression level. The coding tensors for all models in this plot are learned and separable.

able to generate high-quality reconstructions comparable to the no-compression oracle. Overall, optimizing the coding tensors can provide non-trivial performance gains.

What if we could compute depths in-pixel? Fig. 6 compares the depth reconstruction quality of two learned coding tensors at 64x compression with the peak compression oracle described in Sec. 6.1. At high SBR, all methods recover the fine and coarse scene details. At low SBR the peak compression oracle fails to reconstruct high-level scene structures such as the rings in the red box, while the learned coding tensors better preserve these coarse and fine details.

6.3. Exploring the Coding Tensor Design Space

When does spatio-temporal coding help? Fig. 7 shows the effect of increasing the spatial dimension of $\mathbf{C}$, at 64x compression. At high SBR, all methods have similar MAE, but, coding tensors with smaller spatial dimensions better preserve fine details (e.g., sticks). On the other hand, at low SBR, coding tensors with larger spatial dimensions preserve high-level details such as the pot handle. This difference is also observed in the scatter plot where the mean and median of the $256 \times 1 \times 1$ $\mathbf{C}$ do not match which indicates multiple low SBR scenes with high MAE.

How does reducing the size of $\mathbf{C}$ affect performance? Fig. 8 shows the effect of reducing the size of $\mathbf{C}$ at 128x compression. The coding tensors size is reduced by training models with separable coding tensors that operate on smaller histogram blocks. The performance difference between full and separable coding tensors ($1024 \times 4 \times 4$) is negligible. As we further reduce the number of parameters in $\mathbf{C}$, the overall performance degrades. Coding tensors with fewer parameters that operate on smaller histogram blocks tend to produce blurrier reconstructions. This can be observed in the red box where the coding tensors with less than 10,000 parameters blurs the spikes. Nonetheless, as discussed in Sec. 4.1, a parameter-efficient $\mathbf{C}$ is desirable due to the limited in-sensor memory. Ultimately, a practical

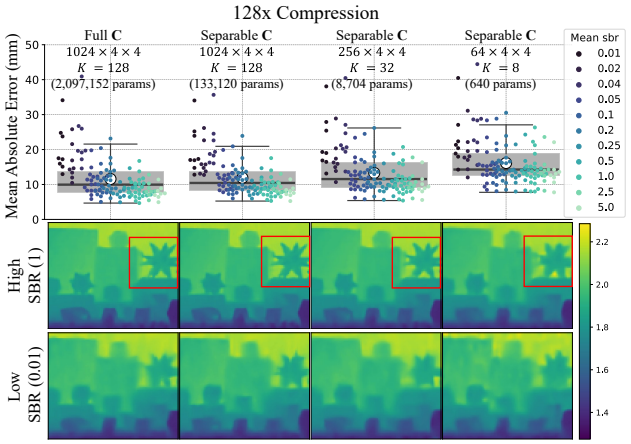

Figure 8. **How does Reducing Size of C Affect Performance?.** Each scatter plot point corresponds to the MAE of a test scene. The images directly below each model correspond to the depth reconstructions for two test scenes at high and low SBR levels whose mean signal and background photons per pixel are [10, 10] and [10, 1000], respectively. The size of $\mathbf{C}$ is reduced from left to right by making it separable or reducing the M_t.

compressive SPAD-based 3D camera design requires determining the trade-off between parameter efficiency and 3D imaging quality, which may depend on the application.

6.4. Evaluation on Real-world Data

Fig. 9 shows the depth reconstructions at 256x compression of multiple compressive histograms and the no compression baseline on the real-world experimental data from [24]. In low SBR scenes, such as the outdoor capture of the ball falling down stairs (first row), Truncated Fourier blurs the staircase edges, while the learned spatio-temporal $\mathbf{C}$ preserved these details. Compared to the no compression oracle, compressive histogram models produce less smooth depth images with some small artifacts. This suggests that the compressive histogram models could benefit from a spatial regularizer such as the one used when training the no compression oracle. Additional results and details on this evaluation are available in the supplement.

6.5. On-chip Implementation and Power Analysis

To validate the feasibility of compressive histograms, we implement them on the UltraPhase chip which has a 3×6 processor core array [4]. At this time, UltraPhase has not been 3D stacked on a SPAD sensor, thus we only evaluate its compute and data readout power consumption. Fig. 10 shows the power dissipated by UltraPhase when processing photon timestamps with different methods and transferring data off-sensor. Although compressive histograms dissipate more power on computation (blue), this is less than 0.3% of the overall power consumption, which is dominated by data readout. Due to limited memory in UltraPhase (4096 bits per core), our method learns $\mathbf{C}^{\text{spatial}}$ and uses Fourier codes

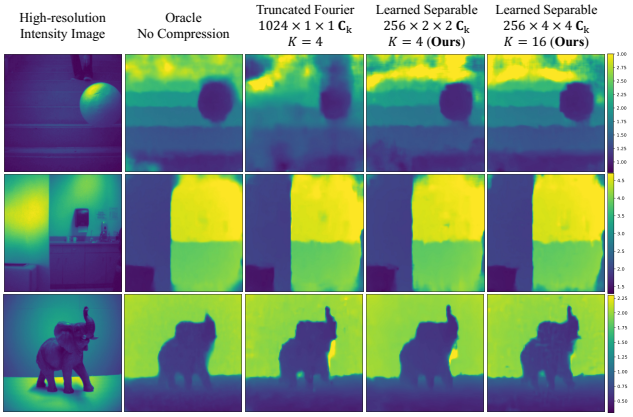

Figure 9. **Depth Reconstructions of Real-world SPAD Data at 256x Compression.** Depth reconstructions of different scenes captured with a SPAD-based 3D camera prototype [24].

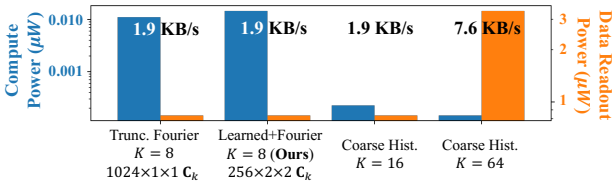

Figure 10. **Compute vs. Data Readout Power.** Average power dissipated by 2x2 SPADs processing 500 timestamps per depth frame and operating at 30 depth frames per second. Compute power is obtained from the implementation on the UltraPhase SPAD processors [4]. Readout power is estimated from the output data rate assuming the readout scheme of the SwissSPAD2 [46]. Coarse histograms use 8-bit precision, while compressive histograms use 16-bit precision. Note the difference in blue and orange scales.

for $\mathbf{C}^{\text{temporal}}$ due to their memory efficient implementation. We also quantize $\mathbf{C}$ to 8 bits and find no degradation in performance. Refer to the supplement for additional details.

7. Discussion

SPAD-based 3D cameras encounter a data bottleneck between the SPAD array and the compute module when transferring the photon timestamps. A histogram tensor can help summarize timestamps at low resolutions, but as megapixel SPAD arrays become available, histogram tensors also lead to a data bottleneck. To overcome this limitation we proposed compressive histograms as a compact representation that can be built on-the-fly, as each photon is detected. As a consequence, compressive histograms can reduce the in-sensor memory and data rates because neither the photon data stream nor a histogram tensor needs to be stored or transferred. Our results show that high-quality depth information can be recovered from a learnt compressive histogram representation that is up to 2 orders of magnitude smaller than a histogram tensor representation.

Practical compressive histogram operating points: The

learned separable 256x4x4 and 256x2x2 $\mathbf{C}$, achieved a good balance between parameter efficiency vs. reconstruction quality, and require on the order of 10-100kbits of memory. In an UltraPhase-like chip this would require distributing $\mathbf{C}$ among at least 8x8 cores (4kbits per core). If the temporal dimension is fixed to Fourier-based $\mathbf{C}^{\text{temporal}}$ such as the ones from [16, 40], the number of parameters can be reduced by 10-40x (see Suppl. Sec. 3.3) which enables storing $\mathbf{C}$ on a per-pixel basis and made the UltraPhase evaluation possible. Overall, for a 1MP SPAD sensor with 1000 bins per-pixel, compressive histograms that can provide more than 50x compression would result in practical data rates of ~ 0.6GB/s which USB 3.2 can support.

Trade-off space: Compressive histograms establish a trade-off between reconstruction fidelity, data bandwidth, and in-sensor compute and memory resources. For a fixed bandwidth, a coarse histogram requires arguably the lowest in-sensor resources but leads to poor reconstructions. Fourier-based histograms can improve reconstruction fidelity, at the expense of increased in-sensor computation and memory. The proposed generalization of compressive histograms allows further increasing reconstruction accuracy, at the expense of additional in-sensor memory over Fourier-based methods. Ultimately, the correct trade-off for a given scenario will be determined by power, application, and hardware constraints.

Although compressive histograms require more in-sensor computation than coarse histograms, our method presents a practical solution from a power consumption and a real-time application perspective. Power consumption is primarily determined by data rates. Fig. 10 and Suppl. Fig. 4 shows that despite compressive histograms dissipating 100x more processing power than coarse histograms, their overall power consumption is still lower even when data rates are only reduced by 2x. The processing time for building compressive histograms is $\sim$0.5ms (Suppl. Fig. 5). From a real-time (*i.e.*, 30 FPS) or a high-speed application standpoint, this additional processing time is nearly negligible since it is overlapped with acquisition/exposure time.

From a hardware perspective, the importance of reducing the memory overhead of $\mathbf{C}$ depends on resolution. In low-resolution SPAD cameras, memory-efficient $\mathbf{C}$ are essential because they are stored among a single or a few pixels. The proposed method allowed integrating memory-efficient Fourier codes with learned spatial codes, which were implemented on the 2x2 pixels of UltraPhase (Suppl. Sec. 2). As resolution increases and $\mathbf{C}$ is shared among more pixels, the memory overhead reduces, and less parameter-efficient $\mathbf{C}$ with increased reconstruction fidelity can be considered.

Bias in Learned $\mathbf{C}$: In the supplement, we show that coding tensors with $M_t = N_t$ develop a depth range bias. These coding tensors learn to zero out photons coming from distances that are less common in the dataset since they are usually background/noise photons. Interestingly, learned coding tensors with $M_t < N_t$ avoid this bias and generalize to depths that are less common in the training set.

Generalization: There are multiple generalization axes including signal and ambient light levels, sensor and laser parameters (*e.g.*, resolution, pulse waveform), and scene response complexity (*e.g.*, depth range, indirect reflections). Our evaluation has probed some of them. Specifically, our training set only included a subset of the signal and ambient light levels that the test set contained. Furthermore, the model was trained and tested on histogram tensors with different resolutions. Finally, the dataset bias investigation showed that models with $N_t \leq 256$ generalized well to less prevalent depths during training (Suppl. Sec. 1).

We further discuss the model's ability to generalize in other scenarios. For instance, all learned models (including baselines) are unlikely to generalize well to wider laser pulses, because if the model is trained with a narrow pulse width, it learns to extract signal information from high frequencies which will only contain noise in the wider pulse. Similarly, these learned models may generalize to narrower pulse widths. Furthermore, we anticipate a learned $\mathbf{C}$ with the properties described in [16] to be robust to diffuse indirect reflections but may require data augmentation to generalize to other light transport scenarios.

Why not compute depths in-sensor? SPAD-based 3D cameras with large in-pixel memory could store per-pixel histograms and reduce data rates by computing depths in-pixel (i.e., peak compression oracle). Our results show that compressive histogram can provide similar reconstruction quality and outperform this method at low SBR without requiring the storage of the full histogram tensor in-sensor.

Additional Coding Tensor Designs: Although we find promising empirical results for the coding tensor representations described in this paper, the optimal set of coding tensors will depend on the exact hardware specifications (e.g, in-pixel memory, system bandwidth) and scene-dependent parameters (e.g., SBR, geometry, albedo). Additional lightweight $\mathbf{C}$ designs could rely on other factorization techniques and weight quantization.

Task-specific Compressive Histograms: Histogram tensors are used in other *active* single-photon imaging modalities such as fluorescence lifetime microscopy [38], non-line-of-sight [12, 26, 32], and diffuse optical tomography [25, 50, 27]. Our framework could be used to find compressive representations optimized for these applications.

Acknowledgments: This work was supported by the Department of Energy and National Nuclear Security Administration (DE-NA0003921), Air Force (FA9550-21-1-0341), Swiss National Science Foundation (200021_166289), and NSF Awards 1846884 (A.V.), 1943149 (M.G.), 2107060 (M.G.), 2138471 (A.I.). U.S. DOE full legal disclaimer: https://www.osti.gov/stip/about/disclaimer.

Supplementary Document for "Learned Compressive Representations for Single-Photon 3D Imaging"

S. 1. Dataset Bias in Learned Coding Tensors with $M_t = N_t$

In this section, we analyze the training dataset depth bias that is embedded in some coding tensor designs, and its effect on generalization to scenes with depths that appear less often in the dataset.

Depth Range Bias in Learned Coding Tensors: Supplementary Figures 1 and 17 visualize the temporal dimension for different coding tensor designs as a matrix. The learned coding tensors that operate on the full temporal dimension (i.e., $M_t = N_t = 1024$) show structure in approximately the first half of the matrix, and in the second half their magnitude is close to 0. According to the coding tensor design heuristics introduced in [16], these coding tensors may have depth ambiguities in the second half of the depth range and may not be robust to noise when estimating depths in that range. These learned coding tensors are consistent with the depth range observed in the NYUv2 training dataset whose depths are concentrated between 0.5-7m (i.e., close to half of the depth range in our simulation) [24]. Our evaluation in the main paper only included test scenes with depths < 7m, therefore, this bias had little impact on the performance. To further analyze the impact of this bias on generalization, in the remainder of this section we evaluate the models on a modified Middlebury test set that contains a global depth offset of 7m, making its depth range 7-10m.

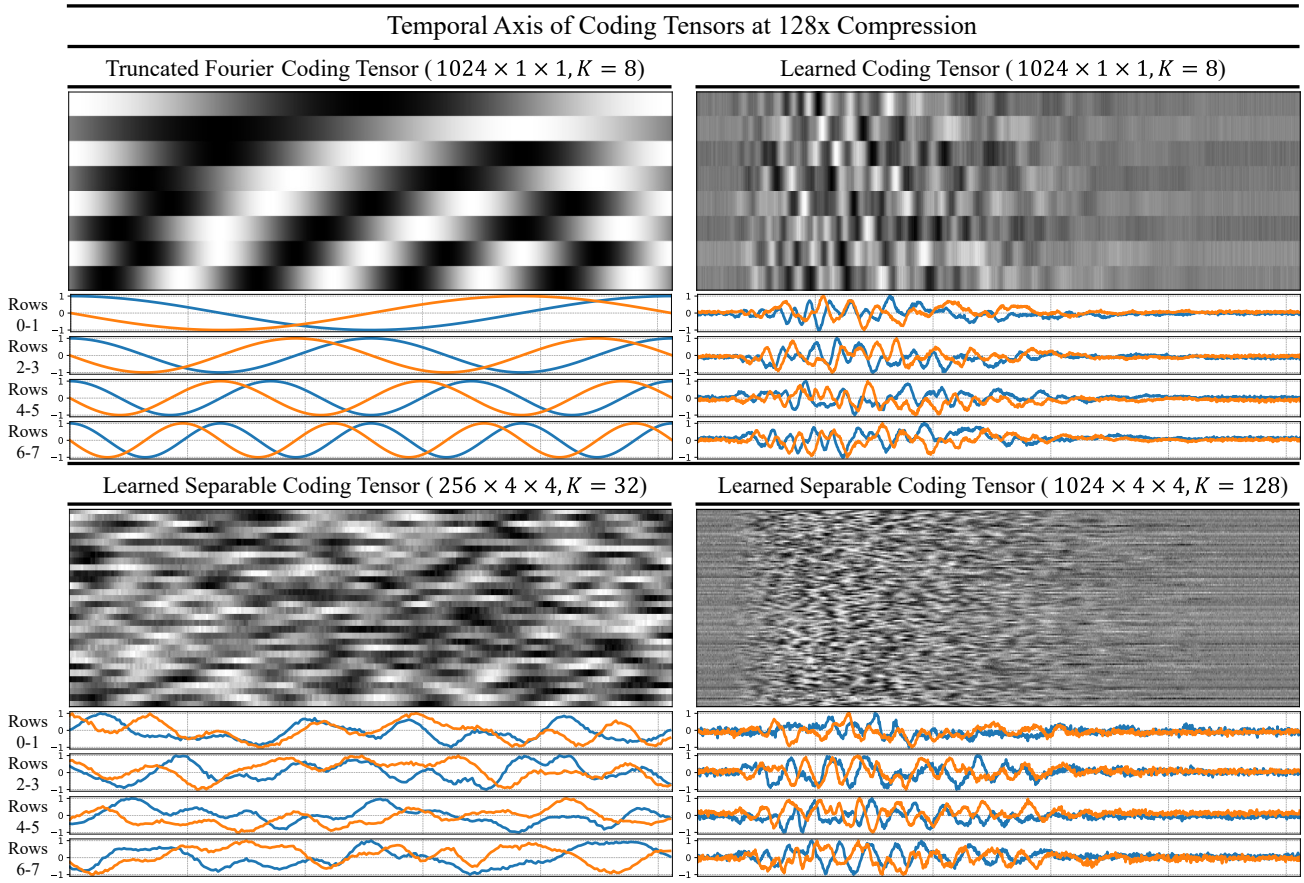

Supplementary Figure 1. **Temporal Dimension of C at 128x Compression** Visualization of the temporal dimension for different coding tensors that achieve 128x compression. The matrix visualized for coding tensors of dimension $1024 \times 1 \times 1$ (columns 1 and 2) is an 8×1024 matrix, since $K = 8$ and $M_t = 1024$. On the other hand, the matrix for the learned separable $256 \times 4 \times 4$ $\mathbf{C}_k$ is 32×256 since $K = 32$ and $M_t = 256$. Similarly, the matrix for the learned separable $1024 \times 4 \times 4$ $\mathbf{C}_k$ is a 128×1024 matrix. The bias on the learned coding tensors with $M_t = 1024$ is displayed on the weights whose magnitude is close to 0 on the right-most side of the matrices. The functions shown below each matrix correspond to different rows of the matrix.

Quantitative Performance Analysis on Depths Between 7-10m: Fig. 2 shows how the performance of different compressive histogram models varies as a function of the compression ratio. The learned coding tensors with $M_t = N_t = 1024$

(i.e, orange and green lines) consistently display poor performance across all compression levels. Moreover, the variance in their MAE is very high which is likely due to generalization artifacts. Fourier-based coding tensors (blue line) continue to achieve reasonable performance at CR < 64 and poor performance for higher compression levels, which is consistent with the results in the main paper. Finally, the learned coding tensor with $M_t < N_t$ (red line) displays good performance across all compression and SBR levels, comparable to the results in the main paper, despite the aforementioned dataset bias.

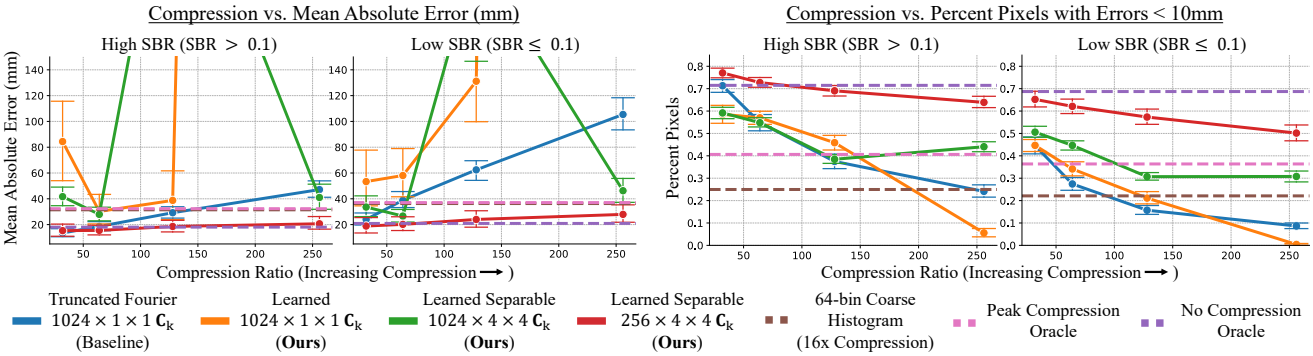

Supplementary Figure 2. **Compression vs. Test Set Metrics on Large Depths Test Set.** Performance on the Middlebury test set with a 7 meter depth offset applied to all depth images before simulation. The two left-most plots show the mean absolute error computed over the test set as we increase compression. Similarly, the two right-most plots show the mean percent of pixels whose absolute depth errors were < 10mm. The simulated test set images were divided into low (SBR ≤ 0.1) and high (SBR > 0.1) SBR groups to be able to disentangle the impact of SBR on the performance of each model. The dashed lines show the peak and no compression baselines whose compression levels do not vary. Each line corresponds to a fixed coding tensor design for which we vary K to control the compression level. Moreover, each point for a given compression level corresponds to a single set of coding tensors jointly optimized with the depth estimation 3D CNN. The learned coding tensors with $M_t = N_t = 1024$ (orange and green lines) show significantly elevated MAE compared to a learned $\mathbf{C}$ with $M_t = 256$. This poor performance is due to the depth reconstruction artifacts observed in Suppl. Fig. 3.

Qualitative Performance Analysis on Depths Between 7-10m: Fig. 3 shows the depth reconstruction for multiple baselines and compressive histograms at 32x and 128x compression. The recovered depth images with learned coding tensors with $M_t = N_t = 1024$ display multiple artifacts at both high (1) and low (0.05) SBR for both scenes. These artifacts explain why we observe elevated MAE in Fig. 2, but at the same time, the percent pixels with errors $< 10mm$ is not incredibly low for some compression levels. On the other hand, the learned separable $256 \times 4 \times 4$ $\mathbf{C}$ not only obtains artifact-free reconstructions but also continues to show the same trends observed in the paper. For instance, at 128x compression and SBR=0.05, it is able to preserve important scene information that is lost when using a Truncated Fourier $\mathbf{C}$.

Summary: In general, it is important to analyze and account for dataset bias in any learning-based model. We find that this bias can lead to learned coding tensors that only work well for a subset of depths. One way to resolve this problem is by augmenting the dataset to include examples with depths for the full depth range. However, we find that an even simpler approach is to consider a coding tensor design that considers a smaller block size, making the tensor convolutional. In this section, we showed that the learned coding tensors that are robust to this dataset bias, continue to provide the same performance benefits that were observed in the main paper.

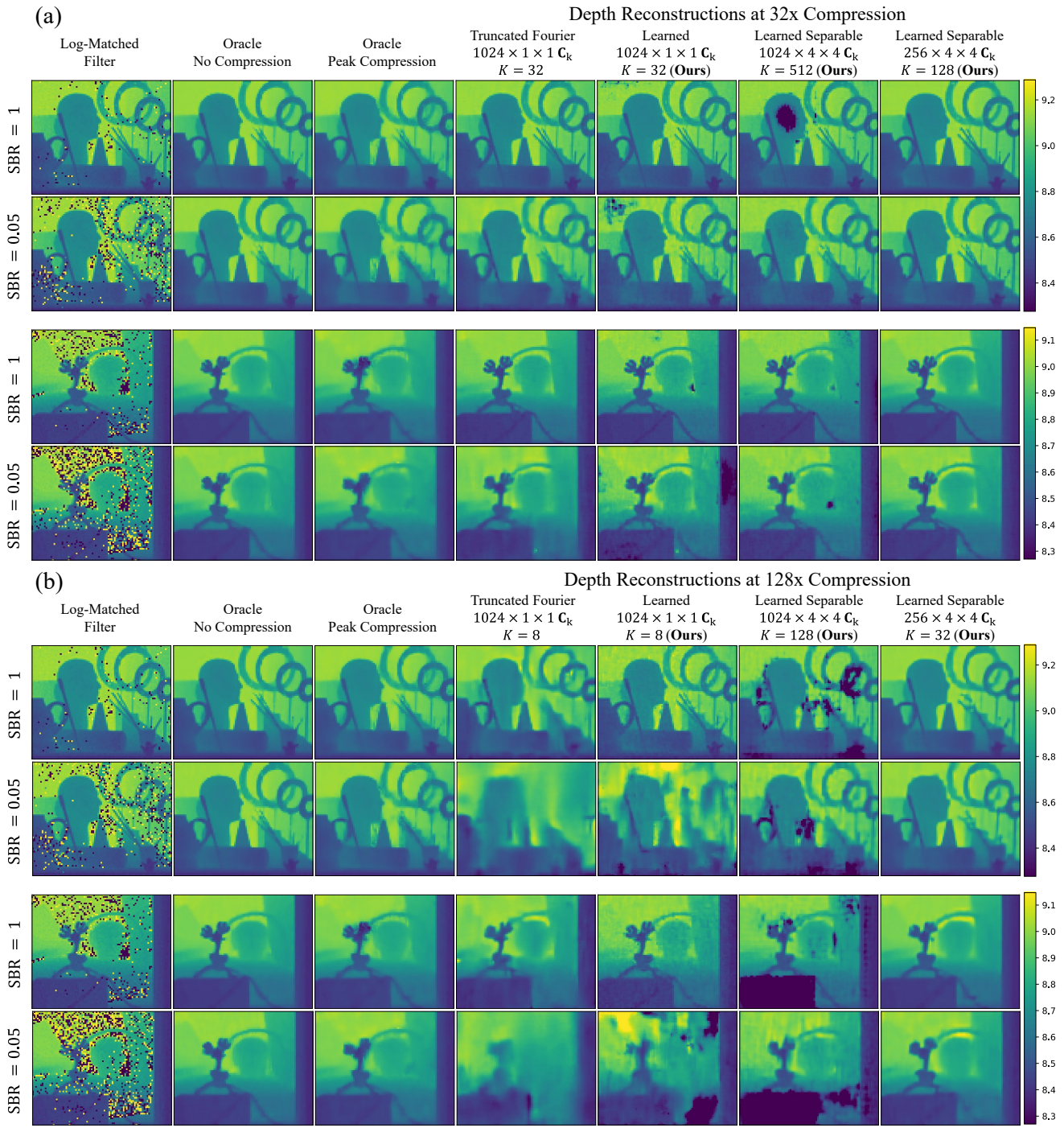

Supplementary Figure 3. **Depth Reconstructions at 32x and 128x Compression for Scenes with Depths Between 7m and 9.5m.** Recovered depths for two scenes whose depths range between 7m and 9.5m. The compressive histogram models achieve 32x (a) and 128x (b) compression. The SBR levels of 1 and 0.05 correspond to a scene simulated with an average number of detected photons per pixel of [10,10] and [10,200]. Learned coding tensors with $M_t = N_t = 1024$ produce reconstructions with multiple artifacts which indicates that they have poor generalization for this range of depths, which is consistent with the observed depth range bias observed in Suppl. Fig. 1.

S. 2. On-chip Implementation and Power Consumption Analysis

In this section, we provide further details on the UltraPhase SPAD chip used for the power analysis, our compressive histograms implementation on it, and a discussion on the role compressive spatio-temporal histograms can play in the scaling of this in-pixel processing architecture to megapixel SPAD-based 3D cameras with picosecond time resolutions.

UltraPhase SPAD Processing Chip [4]: The UltraPhase chip consists of a 3×6 array of processing cores, each connected to 4×4 SPAD pixels resulting in a 12×24 SPAD camera. Every core is independent, and can execute programs of up to 256 instructions in length at a rate of 140 MOPS and has 4096 bits of available RAM. The system supports a wide range of instructions, from logic to 32-bit arithmetic operations, data manipulation, and custom inter-core synchronization and communication. Although the 3×6 array of processing cores has been fabricated, it has not been 3D stacked on the 12×24 SPAD camera *yet*. Therefore, our analysis focuses on the implementation of our proposed methods on the processing cores and their corresponding power consumption, data rates, frame rates, and processing times.

Implementation: In our current implementation, we assume that one UltraPhase processing core is equivalent to a single SPAD pixel, even though each processing core will eventually be connected to 4×4 SPAD pixels. This assumption is made because the current version of UltraPhase does not keep track of the spatial information of a photon timestamp that was detected within the 4×4 region. This assumption will not be necessary for future versions of UltraPhase or UltraPhase-like chips that are able to keep track of the spatial location of a timestamp that was detected within the SPAD region the processing core is connected to (e.g., [48]). Nonetheless, since there are 3×6 cores, we are able to validate the proposed spatio-temporal compressive histograms since we do know the spatial information of a timestamp at the processing core level.

All methods implemented on UltraPhase take as input 10-bit timestamps. A 10-bit timestamp is consistent with the datasets in the main paper where the full-resolution histogram had $N_t = 1024$ bins, i.e., the detected timestamps could take one of 1024 possible values. We implement the following compressive histogram methods on UltraPhase:

1. **K-bin Coarse Histogram:** Coarse histograms are one of the simplest compressive histograms [16]. When a timestamp is detected, its value is used to determine the histogram bin index to increment. Each coarse histogram bin has a bit depth of 8 bits.

2. **Memory-efficient Truncated Fourier ($1024 \times 1 \times 1$ $\mathbf{C}_k$):** A naive implementation of a Truncated Fourier coding tensor would require storing K $1024 \times 1 \times 1$ coding tensors which would not fit in the memory of one UltraPhase core. However, it is possible to compute the values of any Fourier coding tensor from the first quadrant $[0, \frac{\pi}{2}]$ of the cosine and sine functions using trigonometric identities. The first quadrant corresponds to the one-fourth (first 256 elements) of the first row of the Truncated Fourier matrix shown in Fig. 1. This means that all truncated Fourier coding tensors can be generated from only 256 parameters which occupy 2,048 bits of memory when quantized to 8 bits. When a timestamp arrives, its value is used to generate the K Truncated Fourier coefficients, which are aggregated on a 16-bit compressive histogram. Please refer to [4] for further details on this implementation.

3. **Separable Temporal Fourier and Learned Spatial Coding Tensors ($256 \times 2 \times 2$ $\mathbf{C}_k$):** This compressive histogram model uses the proposed separable coding tensors with dimensions $256 \times 2 \times 2$. The spatial coding tensors ($\mathbf{C}_k^{\text{spatial}}$) are learned, while the temporal coding tensors ($\mathbf{C}_k^{\text{temporal}}$) are fixed to truncated Fourier coding tensors with $M_t = 256$. We leverage the same memory-efficient truncated Fourier implementation described above. All coding tensors are quantized to 8 bits. The resulting spatio-temporal coding tensors occupy 768 bits and 1,024 bits of memory for $K = 8$ and $K = 16$, respectively ($(64 + 2 \cdot 2 \cdot K) \cdot 8$bits). For this method, we use 2×2 cores. Each core stores a copy of the temporal coding tensors and its corresponding part of the spatial coding tensor. When a timestamp arrives, its value is used to generate the K coding tensor coefficients that are added to the 16-bit compressive histograms. Each core builds its own compressive histograms and before transferring the data off-sensor the compressive histograms of the 2×2 cores are added and transferred. This implementation could be made more memory-efficient if only a single core keeps track of the compressive histograms.

For the interested reader, we have included the custom assembly implementations of the above methods in the supplementary material.

Why not use a learned $\mathbf{C}_k^{\text{temporal}}$: As shown in Suppl. Sec. S. 3.3, for certain coding tensor designs such as a separable $256 \times 2 \times 2$ $\mathbf{C}_k$, learned temporal coding tensors can outperform truncated Fourier temporal coding tensors. Unfortunately, in our current per-core implementation storing K learned separable $256 \times 2 \times 2$ coding tensors would require $(256 \cdot K + K) \cdot 8$bits of memory per core (16,448 bits for $K = 8$). The next step in this line of work is to start adopting distributed memory implementations where the coding tensors are distributed across multiple neighboring cores to reduce the memory overhead of the coding tensors.

Processing Power Estimation: The UltraPhase chip was characterized by executing specific instructions in an infinite loop and measuring the average power consumption. The measured average power per instruction per core was 1.06e-11 Watts, and one instruction requires 3 clock cycles to execute. To estimate the average power consumption of each of the above methods, their execution time (in clock cycles) is measured, and then we estimate power consumption by assuming the worst-case scenario, when all the operations involve reading and writing to the RAM and power consumption is at maximum. Finally, given an average number of photons per depth frame, we compute the average processing power for a set of 2×2 cores/pixels that outputs 30 depth frames per second. The resulting numbers are summarized in the table on Suppl. Fig. 5.

Data Transfer/Readout Power Estimation: To estimate the data readout power, we assume a conventional digital I/O at 3.3V with a load of 5pF operating at the specified bandwidth. This is the same standard readout interface used by the SwissSPAD2 [46], which is a high-resolution 512×512 SPAD array. Given the data rate, power can be estimated as $\text{DATARATE} \cdot 5 \cdot 10^{-12} \cdot (3.3^2)$, where DATARATE is in units of bits/second.

Power Consumption Analysis: Fig. 4a shows the processing and data readout power consumption. Although compressive histogram models dissipate around 100x more power when processing compared to coarse histograms, the processing power for all methods continues to be only a small fraction of the overall power dissipated. Data readout is the dominant power consumption source, hence reducing data rates can provide higher power reductions than reducing computation.

As observed in Fig. 4b, the proposed spatio-temporal compressive histograms with $K = 16$ can provide comparable depth reconstruction quality to a 256 bin coarse histogram, while reducing data rates and consequently data readout power by 8x. To emulate 8-bit quantization for the compressive histogram models, at test time, we quantize the coding tensors to 8-bits.

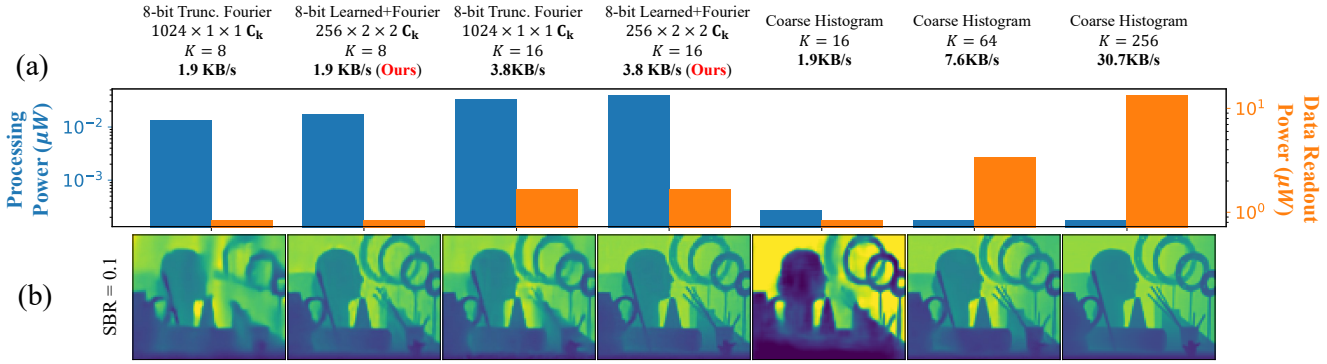

Supplementary Figure 4. **UltraPhase power analysis for 2×2 pixels.** (a) Average power dissipated by 2×2 cores/pixels when processing 550 photon timestamps per pixel per depth frame at 30 frames per second. The processing power is estimated from each methods implementation on 2×2 cores of UltraPhase. The data readout power is estimated from the output data rate and assuming the same readout scheme of the SwissSPAD2 [46]. Coarse histograms have 8-bit precision, while compressive histograms have 16-bit precision, which means that a coarse histogram with twice as many coefficients will have the same data rate. The y-axis is in log scale and is displayed for the processing and readout power independently. (b) Simulated depth reconstructions for each method on a scene with an average of 550 photons detected per pixel (50 signal photons and 500 background photons). The coding tensor weights for the compressive histogram models shown here are quantized to 8-bits at test time.

Limitations of the Implementation and Analysis: For the purposes of this paper, we are able to get important insights from our implementation on UltraPhase which assumes each processing core is equivalent to a SPAD pixel. However, having access to the fine-grained spatial information of each timestamp is crucial to exploit the full potential of our proposed method. For instance, a spatio-temporal coding tensor operating on 4×4 SPAD pixels can store a compact compressive histogram that preserved spatial details, while a coarse histogram that aggregates timestamps from the 4×4 pixels will lose the spatial information.

Scaling to Megapixel SPAD Arrays: In an UltraPhase-like architecture, the amount of memory per core is unlikely to significantly increase as we scale to megapixel SPAD arrays due to pixel pitch reasons. Currently, the processing core is 107x107 microns and memory covers around 30% of that area [4]. The pixel pitch for the 4×4 SPADs connected to a core is 28 micron. However, as we scale the megapixel SPAD arrays the pixel pitch will reduce, which means the processing core area will also reduce or it will operate on a larger number of SPAD pixels. Alternatively, the processing core can reduce in size by reducing its computation capabilities (e.g., MegaPhase cores in [4] are 55x55 microns). Therefore, as we scale towards megapixel SPAD processing arrays, we can expect the shared memory across a neighborhood of SPAD pixels to be on the order UltraPhase per-core memory. This extreme memory constraint can inform and further motivate exploring more lightweight coding tensor designs and reducing their memory overhead through distributed memory implementations.

Coding Tensor Model	Compressive Histogram Length (K)	Compressive Histogram Coefficient Bit-Depth	Processing Time Per Photon [clock cycles]	Data Readout Per Pixel/Core Per Frame [Bytes]	Processing Time Per Frame with 550 Photons [seconds]	Data Rate at 30fps [KB/second]	Average Processing Power at 30fps [micro Watts]	Estimated Readout Interface Power [micro Watts]
Coarse Histogram (16 bins)	$K = 16$	8-bits	30	16	3.93e-05	1.92	2.74e-04	0.84
Coarse Histogram (64 bins)	$K = 64$	8-bits	24	64	3.14e-05	7.68	1.75e-04	3.35
Coarse Histogram (256 bins)	$K = 256$	8-bits	24	256	3.14e-05	30.72	1.75e-04	13.38
8-bit Truncated Fourier $1024 \times 1 \times 1$	$K = 8$	16-bits	210	16	2.74e-04	1.92	1.34e-02	0.84
8-bit Truncated Fourier $1024 \times 1 \times 1$	$K = 16$	16-bits	330	32	4.32e-04	3.84	3.32e-02	1.67
8-bit Learned + Fourier (**Ours**) $256 \times 2 \times 2$	$K = 8$	16-bits	241	16	3.15e-04	1.92	1.76e-02	0.84
8-bit Learned + Fourier (**Ours**) $256 \times 2 \times 2$	$K = 16$	16-bits	361	32	4.73e-04	3.84	3.98e-02	1.67

Supplementary Figure 5. **UltraPhase power analysis for 2×2 cores processing 550 photons per depth frame at 30 frames per second.** This table shows the processing time and data rates for different methods and computes the average processing power and the estimated data readout power. One clock cycle is 2.38ns in duration, and single instruction executes in 3 clock cycles. The processing time per frame is obtained by NUM_PHOTONS*PROCESSING_TIME_PER_PHOTON*2.38ns. If we operate at 30 fps, that means that the total exposure time per depth frame is 33ms, and then we are only dissipating processing power for a subset of the 33ms. Hence the average processing power at 30 fps will be given by scaling the processing power by the processing time and then dividing by 33ms.

S. 3. Supplemental Analysis of the Coding Tensor Design Space

In this section, we present additional results related to the ablation study on the coding tensor design space. These results include the effect of the spatial block dimensions, the effect of the size of $\mathbf{C}$, and the performance difference between coding tensors whose temporal dimension is learned vs coding tensors whose temporal dimension is initialized and fixed to truncated Fourier codes.

S. 3.1. When does spatio-temporal coding help?

Figures 6 and 7 show the quantitative and qualitative performance of learned separable coding tensors as we vary their spatial block dimension from 1×1 up to 8×8. At low compression (32x) and high SBR levels, all models are able to produce high-quality reconstructions that recover both coarse and fine details of the scene. At low compression (32x) and extremely low SBR, models with a spatial block larger than 1×1 are able to better preserve some of the coarser scene details such as the sticks. However, quantitatively, the overall performance difference is small. At high compression and high SBR, models with a 2×2 and 4×4 spatial block are able to recover fine details that are blurred in the 8×8, which are particularly noticeable in Fig. 7. Finally, in the most challenging scenario where we have high compression and low SBR, it becomes essential to use a coding tensor that aggregates information from neighboring spatial locations. In this scenario, although all methods blur some fine scene details, the coding tensors with large spatial dimensions better preserve coarser details such as the pot handle and the sticks.

Why does $256 \times 1 \times 1$ fail at 128x compression? As observed in Fig. 6, the coding tensor with dimensions $256 \times 1 \times 1$ fails when only $K = 2$ coding tensors are learned. Although, it is possible to reconstruct depths from a compressive histogram with as few as 2 coded projections [16], finding two coding tensors that can lead to an unambiguous depth range without further regularization can be challenging.

Summary: Overall, coding tensors that exploit spatial correlations are more robust to low SBR settings. However, at high SBR, operating in a large spatial neighborhood can make it harder to resolve fine scene details. Moreover, increasing the spatial block dimension further increases the number of parameters of the coding tensor which, as discussed in the main paper, is less practical. In this analysis, we find that coding tensors with spatial block of 2×2 and 4×4 achieve good balance of robustness to noise at low SBR, while being able to reconstruct fine scene details at high SBR.

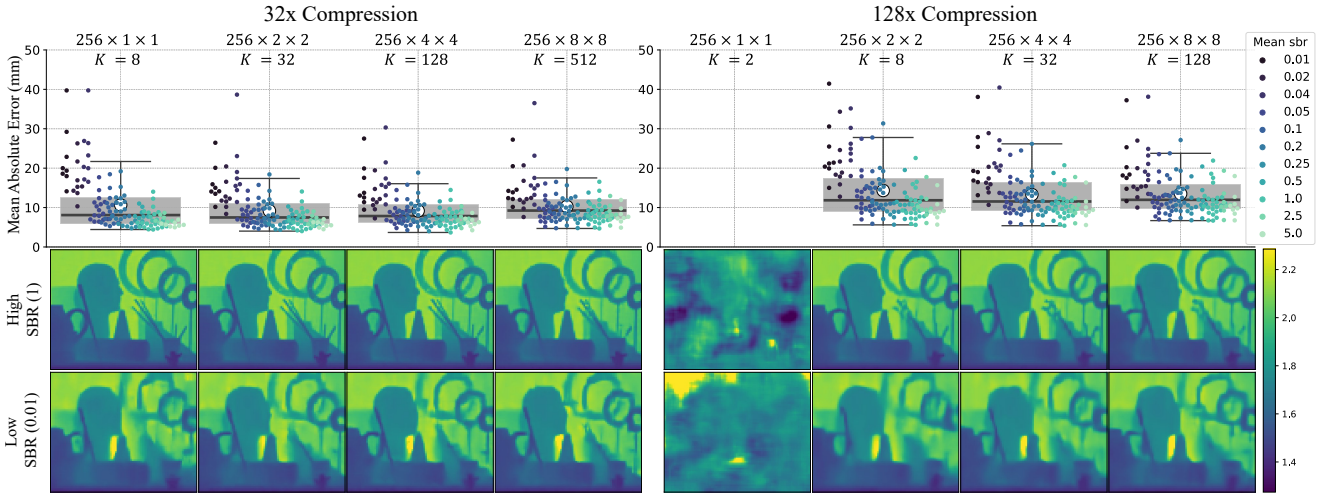

Supplementary Figure 6. **Effect of Spatial Tensor Dimension for $M_t = 256$** Each point in the scatter plots show the MAE for a given test scene and their color hue represent the mean SBR level used in that simulation. The horizontal black line, white circle, gray box, and error bars correspond to the median, mean, quartiles, and 1.5x the inter-quantile range, respectively. Outliers with an MAE larger than 50mm are not visible in the plot, however, they are included in the calculation of the statistics. The images directly below each model correspond to the depth reconstructions for two test examples at low and high SBR levels whose mean signal and background photon detections per pixel are [10, 10] and [10, 1000], respectively. For a fixed compression level, the spatial block size of each model is increased from left to right and K is adjusted to maintain the same compression level. The coding tensors for all models in this plot are learned and separable for spatial blocks larger than 1×1.

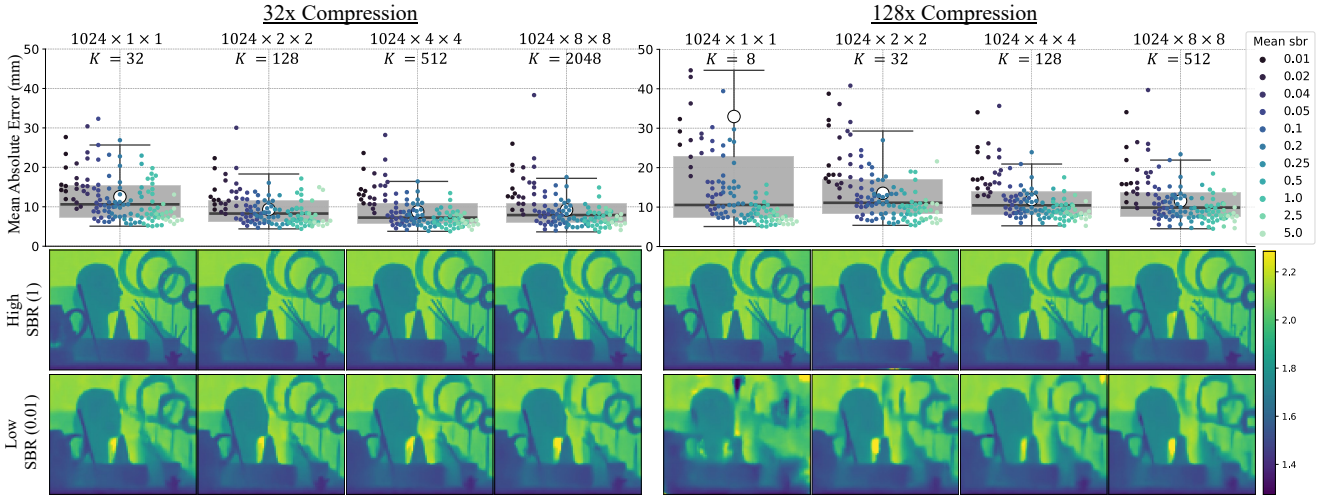

Supplementary Figure 7. **Effect of Spatial Tensor Dimension for** $M_t = 1024$ Each point in the scatter plots show the MAE for a given test scene and their color hue represent the mean SBR level used in that simulation. The horizontal black line, white circle, gray box, and error bars correspond to the median, mean, quartiles, and 1.5x the inter-quantile range, respectively. Outliers with an MAE larger than 50mm are not visible in the plot, however, they are included in the calculation of the statistics. The images directly below each model correspond to the depth reconstructions for two test examples at low and high SBR levels whose mean signal and background photon detections per pixel are [10, 10] and [10, 1000], respectively. For a fixed compression level, the spatial block size of each model is increased from left to right and K is adjusted to maintain the same compression level. The coding tensors for all models in this plot are learned and separable for spatial blocks larger than 1×1.

S. 3.2. How does reducing the size of the coding tensor affect accuracy?

Figures 8, 9, and 10 show the quantitative and qualitative performance of different learned coding tensors as we reduce the number of parameters from left to right. The number of parameters is reduced by either making the coding tensors separable or making their temporal dimension smaller. At low compression levels (32x compression), coding tensors with as few as 2,560 parameters perform comparably to larger coding tensors with 100x more parameters. At higher compression levels (128x compression), the size of the coding tensors starts having a more pronounced effect on depth image quality. At higher SBR levels (i.e., $SBR \geq 0.1$), the larger coding tensors are able to better recover fine scene structures such as the spikes in Fig. 8 or the toy reindeer antlers in 10. Nonetheless, coding tensors with as few as 8,704 parameters can continue to perform comparably to coding tensors with millions of parameters.

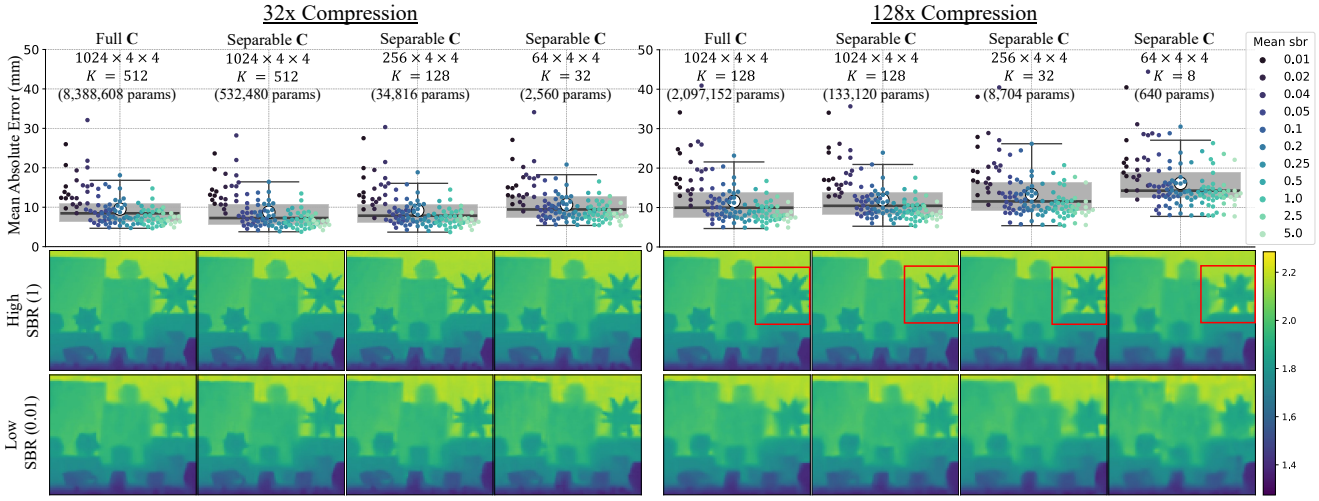

Supplementary Figure 8. **How does Reducing Size of C Affect Performance?.** Each point in the scatter plots show the MAE for a given test scene and their color hue represent the mean SBR used in that simulation. The horizontal black line, white circle, gray box, and error bars correspond to the median, mean, quartiles, and 1.5x the inter-quantile range, respectively. Outliers with an MAE larger than 50mm are not visible in the plot, however, they are included in the calculation of the statistics. The images directly below each model correspond to the depth reconstructions for two test examples at low and high SBR levels whose mean signal and background photons per pixel are [10, 10] and [10, 1000], respectively. For a fixed compression level, the size of the coding tensors is reduced from left to right by making the coding tensors separable and also reducing the temporal dimension. All coding tensors are learned.

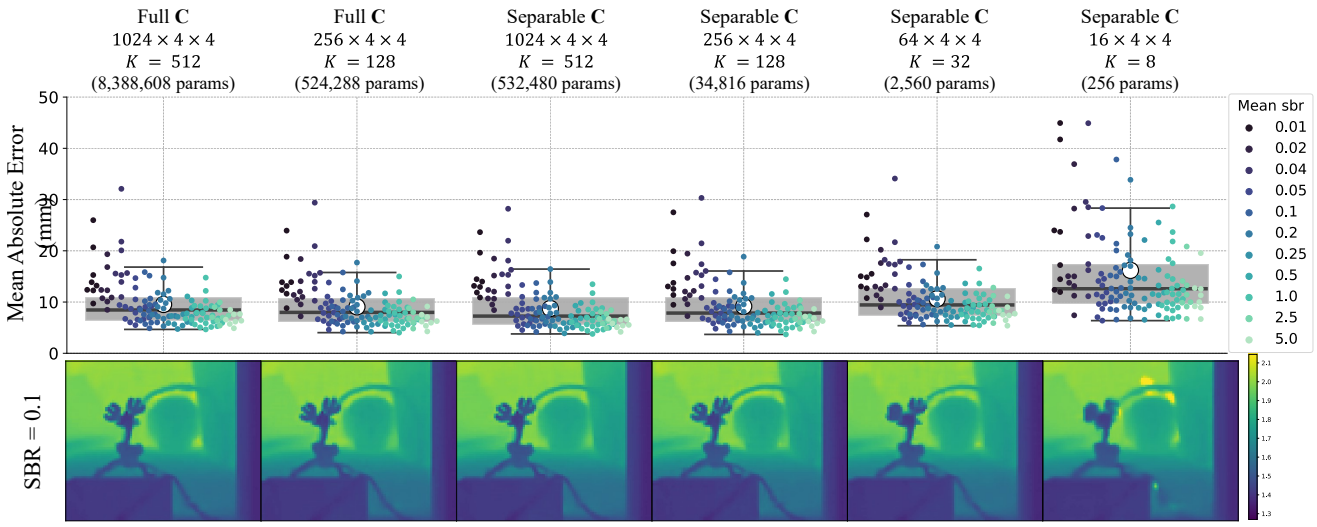

Supplementary Figure 9. **How does Reducing Size of C Affect Performance at 32x Compression?** Each scatter plot point corresponds to the MAE for each test scene. The depth images directly below each model correspond to the reconstruction of one test scene whose mean signal and background photons per pixel are [50, 500]. The size of the coding tensors is reduced from left to right by making the coding tensors separable and also reducing the temporal dimension.

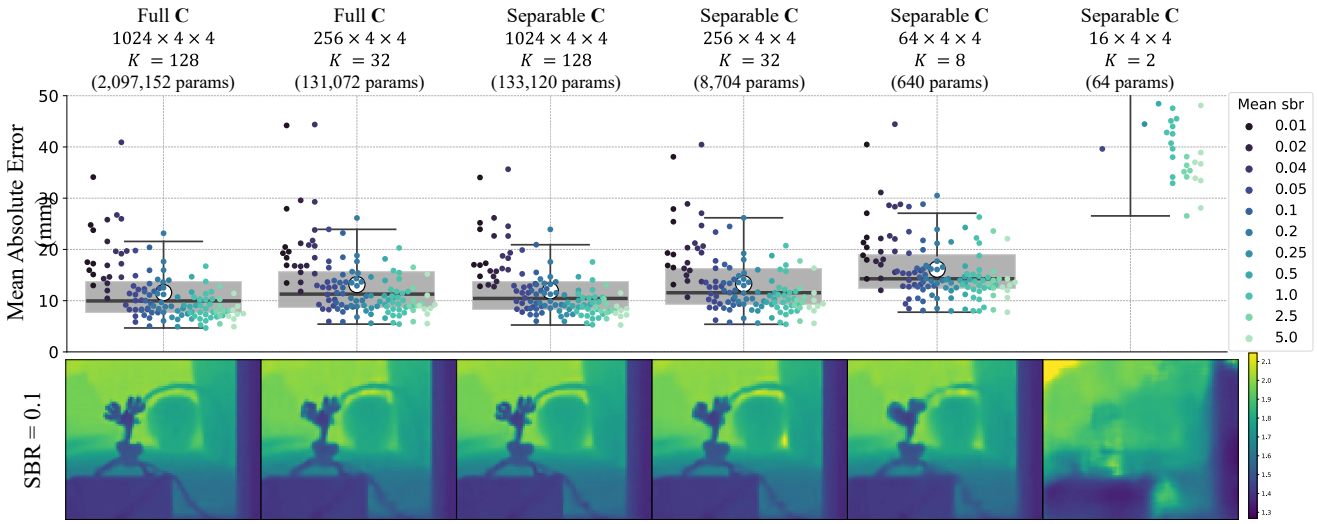

Supplementary Figure 10. **How does Reducing Size of C Affect Performance at 128x Compression?** Each scatter plot point corresponds to the MAE for each test scene. The depth images directly below each model correspond to the reconstruction of one test scene whose mean signal and background photons per pixel are [50, 500]. The size of the coding tensors is reduced from left to right by making the coding tensors separable and also reducing the temporal dimension.

S. 3.3. Learned vs. Fourier-based Temporal Compressive Representations

In this section, we compare the performance of separable coding tensors whose $\mathbf{C}_k^{\text{temporal}}$ is either learned or fixed to a truncated Fourier coding tensor during training.

Temporal Gray Fourier C [16]: In addition to comparing with the Truncated Fourier coding tensors proposed in [40], we also compare against another Fourier-based coding tensor design proposed in [16], which we refer to as Gray Fourier. A Gray Fourier compressive histogram uses coding tensors with dimensions $1024 \times 1 \times 1$. The coding tensors are a Fourier matrix where every two rows the frequency of the sinusoidal signal doubles as illustrated in Suppl. Fig. 17. Similar to our proposed approach, this $\mathbf{C}$ is implemented as a compressive histogram layer, with fixed weights, whose outputs are processed by the depth estimation 3D CNN.

Fourier + Learned C: In this separable coding tensor design, the temporal coding tensors ($\mathbf{C}_k^{\text{temporal}}$) are fixed to truncated Fourier coding tensors, and the spatial coding tensors ($\mathbf{C}_k^{\text{spatial}}$) are learned. The temporal coding tensors in this design can be represented with a small number of parameters that do not scale with K as discussed in Suppl. Sec. S. 2, hence, the in-sensor memory overhead they introduce is smaller than a fully learned coding tensor.

Results: Supplementary Figures 11 and 12 show the overall test set performance and qualitative depth reconstructions for multiple compressive histogram models at 64x and 128x compression, respectively. As discussed in previous sections, coding tensors that exploit spatial information (e.g., $256 \times 4 \times 4$ or $256 \times 2 \times 2$) provide higher quality reconstructions, especially, at lower SBR levels. At 64x compression (Suppl. Fig. 11), models with Fourier or learned $\mathbf{C}_k^{\text{temporal}}$ perform comparably at all SBR levels. At 128x compression (Suppl. Fig. 12), a fully learned coding tensor with dimensions $256 \times 2 \times 2$ can provide some performance improvements for low SBR scenes over the Fourier + Learned $256 \times 2 \times 2$ coding tensor. Nonetheless, at 128x compression, the $256 \times 4 \times 4$ coding tensors provide the best performance.

Summary: Fourier-based temporal coding tensors have a memory-efficient implementation that does not scale with K. Using our flexible spatio-temporal compressive histogram framework, we can design coding tensors whose temporal dimension is fixed to Fourier codes and the spatial coding tensors are learned. This results in a practical compressive histogram model that can be implemented in existing SPAD pixels as shown in Suppl. Sec. S. 2 while providing robust performance across SBR and compression levels. Fully learned coding tensors can still provide some improvements in the most challenging situations (high compression and low SBR), however, they require additional in-sensor memory. Nonetheless, this additional in-sensor memory may be negligible in implementations where a large number of SPAD pixels share the same copy of the coding tensors.

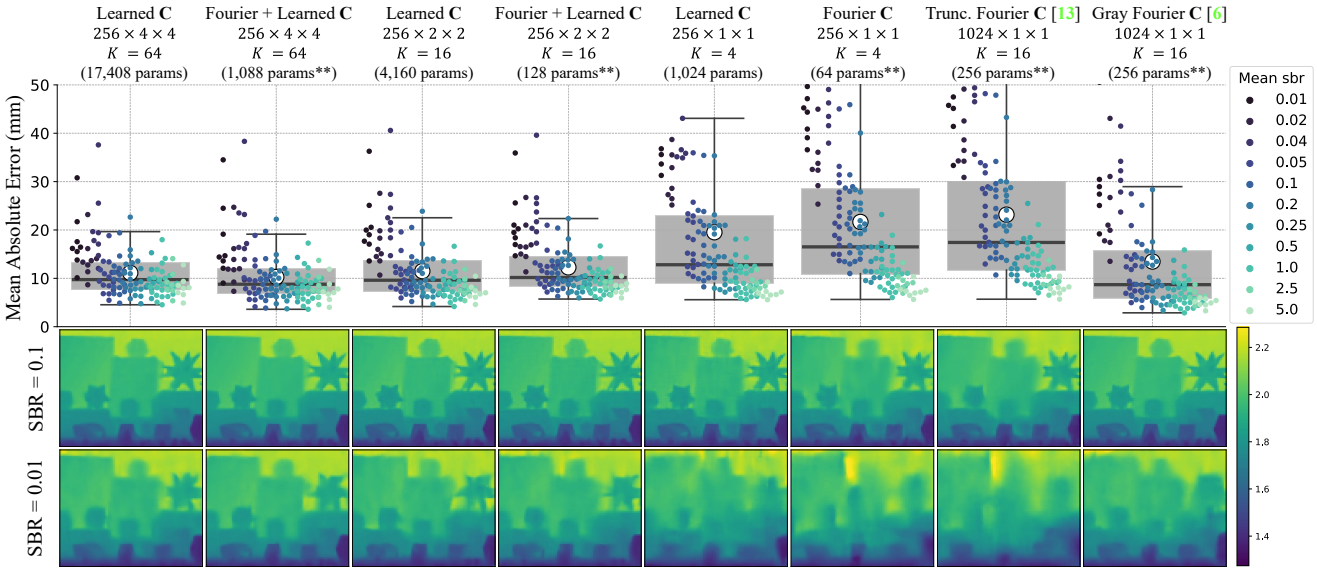

Supplementary Figure 11. **Learned vs. Fourier Temporal Coding Tensors at 64x Compression.** Each scatter plot point corresponds to the MAE for each test scene. The depth images directly below each model correspond to the reconstruction of one test scene whose mean signal and background photons per pixel are [50, 500] and [10, 1000]. All models use separable coding tensors. **The number of parameters for all coding tensors based on Fourier codes is calculated assuming the memory efficient representation described in Suppl. Sec. S. 2.

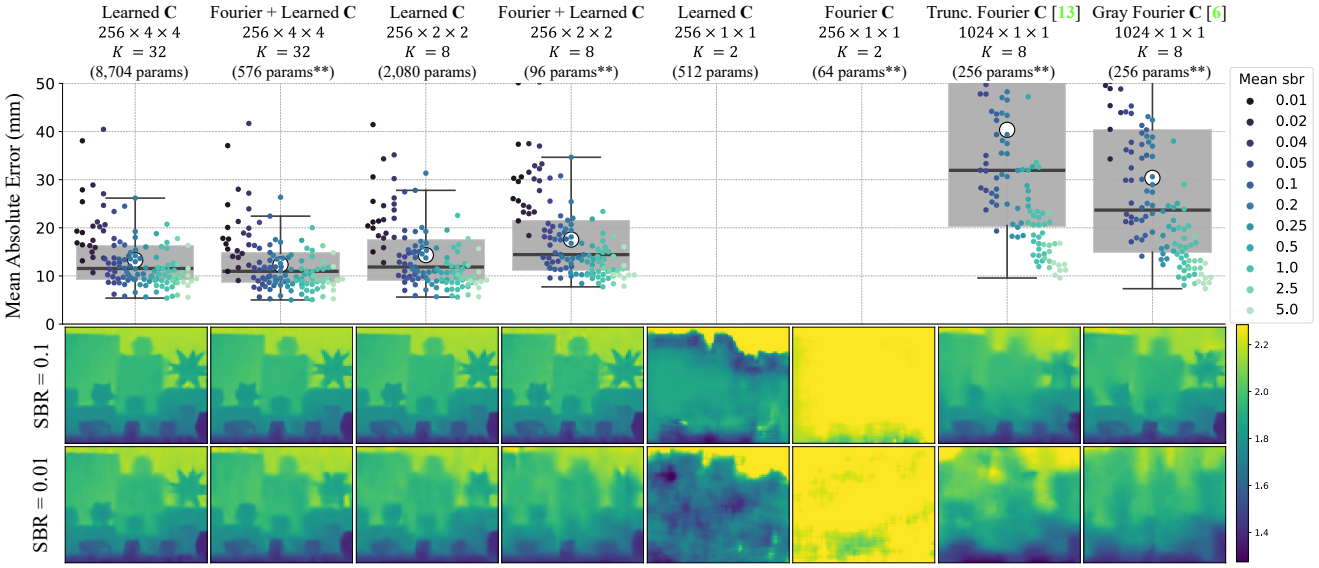

Supplementary Figure 12. **Learned vs. Fourier Temporal Coding Tensors at 128x Compression.** Each scatter plot point corresponds to the MAE for each test scene. The depth images directly below each model correspond to the reconstruction of one test scene whose mean signal and background photons per pixel are [50, 500] and [10, 1000]. All models use separable coding tensors. **The number of parameters for all coding tensors based on Fourier codes is calculated assuming the memory efficient representation described in Suppl. Sec. S. 2. The models trained with $256 \times 1 \times 1$ coding tensors at this compression level are not able to converge and are not able to learn how to reconstruct the scene. This is likely due to the fact that only $K = 2$ coding tensors are used, which as discussed in Suppl. Sec. S. 3.1, can make the optimization challenging.

S. 4. Evaluation on Real-world Data

To evaluate the generalization of the proposed models, we downloaded raw histogram tensor data captured by [24] with a SPAD-based 3D camera prototype. The dataset was captured with a line scanning system composed of a co-located picosecond laser and a 1D LinoSPAD array with 256 SPAD pixels [8]. The histogram tensors have $N_t = 1536$ time bins, a spatial resolution of 256×256, and a bin size $\Delta = 26$ps. The raw histogram tensors are downsampled to be $1024 \times 128 \times 128$ to make the time domain compatible with the learned coding tensors that use $M_t = 1024$ and also to avoid out-of-memory errors.

Fig. 13 and 14 show the depth reconstructions for the oracle baselines and multiple compressive histograms at 256x and 128x compression, respectively. All models are able to produce plausible depth reconstructions, suggesting good generalization to real-world data. However, all compressive histogram models display small artifacts throughout the image that could be due to high noise levels or generalization problems. These artifacts seem to be avoided by the oracle baselines (no compression and peak compression) by over-smoothing the images. This over-smoothing is due to the total variation regularizer that we used for the oracle baselines but not for the compressive histogram models, which we found produced the better oracle models on the synthetic datasets. Therefore, these results suggest that a spatial regularizer can be used to improve the compressive histogram model's generalization on real-world data. Nonetheless, despite these minor artifacts, the depth reconstructions suggest good generalization by all models to these challenging scenarios.

Comparison with Fourier-based $\mathbf{C}$: We observe that the models that used a Gray-based Fourier or a Truncated Fourier $\mathbf{C}$ produced blurrier depth reconstructions than the learned $\mathbf{C}$ models. This can be observed at 128x compression in the lamp scene where the wires merge into a single blob, or in the staircase scene where the stair edges are blurred. At 256x compression, the blurring in the staircase scene is even more significant, likely due to low SBR since the scene is outdoors. On the other hand, the models with a learned $\mathbf{C}$ produce sharper depth reconstructions at the same compression level, despite being trained in the exact same manner.

Comparison with Coarse Histogramming: Although, the depth images for the coarse histogramming coding tensor shown in Fig. 14 look reasonable qualitatively, they have large absolute depth errors when comparing them to the other approaches. A coarse histogram will often produce a quantized depth image [40, 16], however, the depth estimation 3D CNN learns to smooth and upsample the coarse histogram and produce more plausible depth images. Nonetheless, coarse histograms consistently produce less accurate depth reconstructions than other compressive histogram approaches.

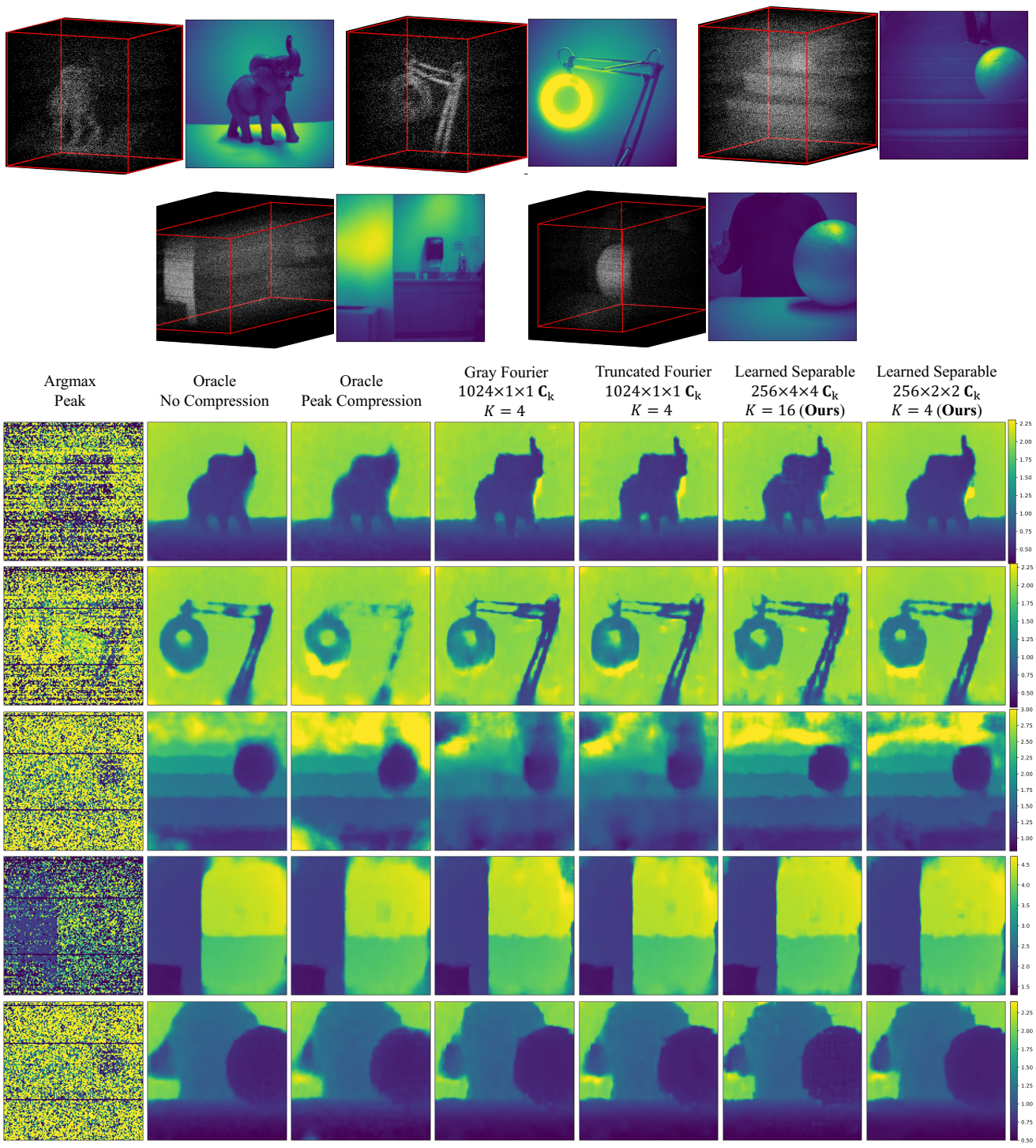

Supplementary Figure 13. **Depth Reconstructions of Real-world SPAD Data at 256x Compression.** Depth reconstructions of different scenes captured with a SPAD-based 3D camera prototype [24]. The first two rows show a high-resolution intensity image of the captured scene and a point cloud visualization of the raw histogram tensor of that same scene. Gray Fourier and Truncated Fourier correspond to the compressive histogram methods proposed in [16] and [40], respectively. For more details on these methods see Suppl Sec. S. 3.3.

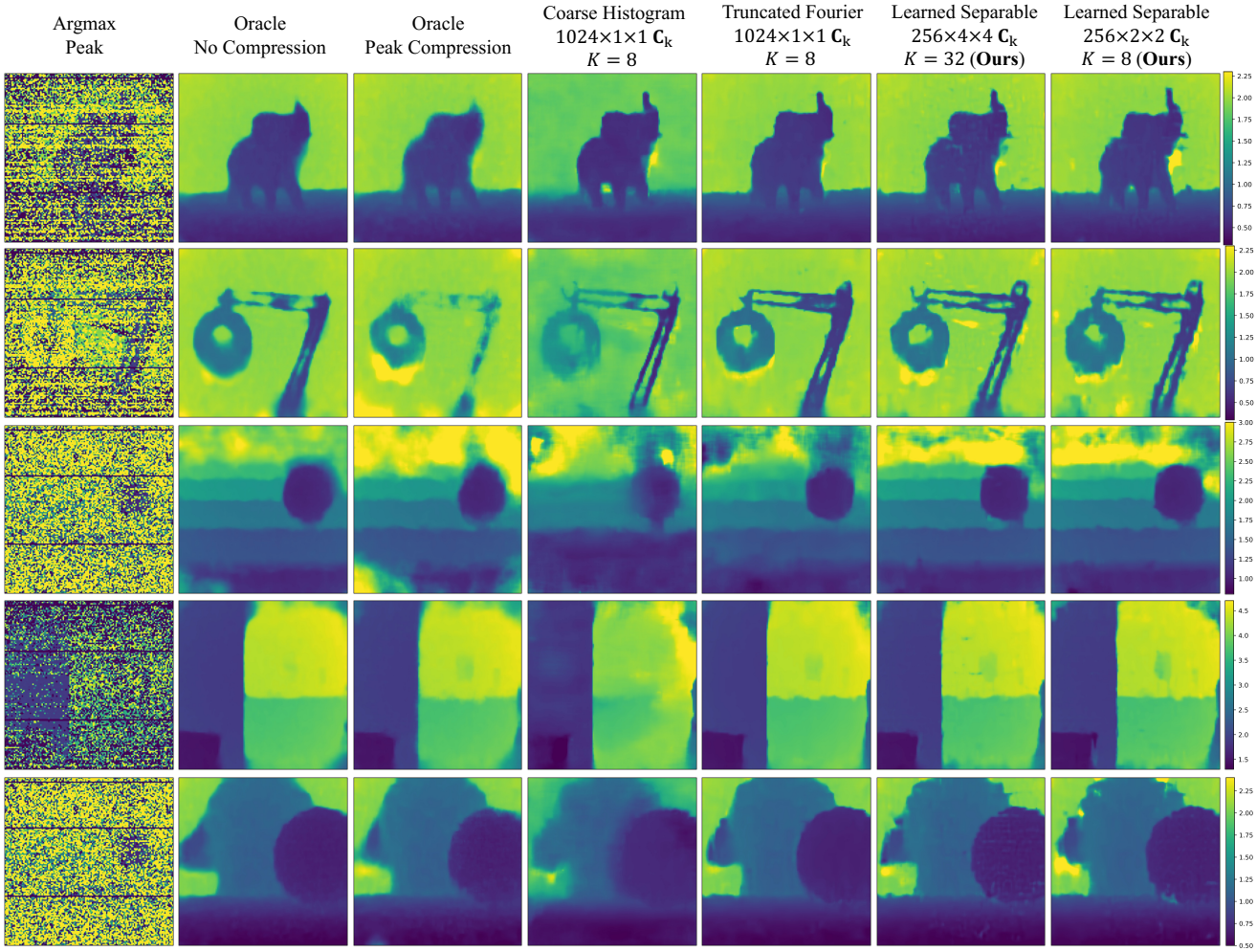

Supplementary Figure 14. **Depth Reconstructions of Real-world SPAD Data at 128x Compression.** Depth reconstructions of different scenes captured with a SPAD-based 3D camera prototype [24]. The two rows show a high-resolution intensity image of the captured scene and a point cloud visualization of the raw histogram tensor of that same scene.

S. 5. Further Datasets and Implementation Details

S. 5.1. Simulating SPAD Measurements

In this section, we provide a detailed description of how SPAD measurements are simulated for the synthetic datasets used in this paper.

Given an RGB-D image, pulse waveform ($h(t)$), and the mean number of detected signal ($\Phi^{\text{sig}}_{\text{mean}}$) and background ($\Phi^{\text{bkg}}_{\text{mean}}$) photons per pixel, we set the photon detection parameters for Eq. 2 as follows. First, we calculate the amplitude of the illumination signal arriving at each pixel ($a_{\boldsymbol{p}}$ in Eq. 1) by using the reflectance at that pixel and accounting for the intensity radial fall-off due to distance. Similar to [24, 36], the NYUv2 training set reflectance was estimated using intrinsic image decomposition on the blue channel of the RGB image, and the Middlebury testing set reflectance was estimated using the mean of the RGB channels. Intrinsic image decomposition can lead to more accurate reflectance estimates for non-lambertian surfaces. Consequently, given $a_{\boldsymbol{p}}$, $h(t)$, the per-pixel depths, and the average number of signal photon per pixel, we can scale the average number of signal photons arriving at each time bin such that $\sum_{\boldsymbol{p}} \sum_i \Phi^{\text{sig}}_{i,\boldsymbol{p}} = \Phi^{\text{sig}}_{\text{mean}}$. Similarly, we can emulate the per-pixel background illumination (Φ^{bkg}) using the RGB channel mean and scaling it such that it matches the desired mean number of background photons per pixel. Finally, we can add dark counts to the per-pixel background illumination component. This step is only done on the training set using a calibration dark count image obtained from the hardware prototype in [24]. We observe that the models trained with this dark count component generalize well to histogram tensors without the dark counts, as shown in our test results.

Summary: Overall, the SPAD measurement simulation pipeline used in this paper is the one originally developed by [24], and later used in [36, 44]. The only significant difference is that our simulated test set includes additional mean signal and background photon count settings.

S. 5.2. Training and Implementation Details

In this section, we provide further training and implementation details.

All models in this paper are implemented in PyTorch [34]. The input to all the models is a 3D histogram tensor. Recall that due to the linearity of compressive histograms, encoding the histogram tensors is equivalent to encoding each individual photon timestamp and summing them up. Hence, models deployed with a compressive histogram layer can also take as input a stream of photon timestamps and build the compressive histogram.

Compressive Histogram Layer: The compressive histogram layer is implemented as a single-layer encoder and decoder. The encoder is a 3D convolution with a stride equal to the filter size. The coding tensors, $\mathbf{C}_k$, are the learned filters. All coding tensors are constrained to be zero-mean along the time dimension. This constraint makes the expected encoded value for background photons distributed uniformly along the time dimension be 0 [40]. The outputs of the encoder are the compressive histograms $\widehat{\boldsymbol{Y}}_b$. The decoder is an unfiltered backprojection that is implemented as a 3D transposed convolution with a stride equal to its filter size.To help the CNN model generalize to different photon count levels we apply zero-normalization along the channel dimension (i.e., K) to the inputs ($\widehat{\boldsymbol{Y}}_b$) and the weights ($\mathbf{C}$) of the transposed convolution as follows:

$$\text{ZN}(\widehat{\boldsymbol{Y}}_b) = \frac{\widehat{\boldsymbol{Y}}_b - \mathbb{E}(\widehat{\boldsymbol{Y}}_b)}{\left\| \widehat{\boldsymbol{Y}}_b - \mathbb{E}(\widehat{\boldsymbol{Y}}_b) \right\|_2}, \quad \text{ZN}(\mathbf{C}) = \frac{\mathbf{C} - \mathbb{E}(\mathbf{C})}{\|\mathbf{C} - \mathbb{E}(\mathbf{C})\|_2} \tag{7}$$

where the mean and L2 norm are computed over the channel dimension. This normalization is also known as layer normalization [5]. Eq. 7 is inspired by the zero-normalized cross-correlation depth decoding algorithm used in ToF imaging [17, 15, 16] and structured light [29, 9].

Depth Estimation 3D CNN Model: To estimate depths from the decoded histogram tensor we use the 3D deep boosting CNN model proposed by [36] for single-photon 3D imaging. Different from [36], our implementation does not include a non-local block after the feature extraction stage. The output of the model is a denoised histogram tensor, $\boldsymbol{H}^{\text{out}}$, from which depths are estimated using a softargmax function along the time dimension. Similar to [24, 36] we use the pixel-wise Kullback-Leibler (KL) divergence between the denoised histogram tensor and a normalized ground truth histogram tensor, $\boldsymbol{H}^{\text{gt}}$, as our objective function. This loss can be written for each pixel, $\boldsymbol{p}$, as:

$$L_{\text{KL}}(\boldsymbol{H}^{\text{gt}}_{\boldsymbol{p}}, \boldsymbol{H}^{\text{out}}_{\boldsymbol{p}}) = \sum_{i=0}^{N_t-1} \boldsymbol{H}^{\text{gt}}_{i,\boldsymbol{p}} \log \left(\frac{\boldsymbol{H}^{\text{gt}}_{i,\boldsymbol{p}}}{\boldsymbol{H}^{\text{out}}_{i,\boldsymbol{p}}} \right) \tag{8}$$

Training: At each training iteration we randomly sample patches of size $1024 \times 32 \times 32$ from the training set. We train all models using the ADAM optimizer [22] with default parameters ($\beta_1 = 0.9, \beta_2 = 0.999$), batch size of 4, and an initial learning rate of 0.001 that decays by 0.9 after every epoch. We train all models for 30 epochs with checkpoints every half an epoch, and for a given model we choose the checkpoint that achieves the lowest root mean squared error (RMSE) on the validation set.

S. 6. Analysis of the Memory Overhead of Coding Tensors

Compressive histograms have the potential to greatly reduce off-sensor data transmissions and the amount of in-sensor memory required compared to a conventional histogram tensor representation. However, the general compression framework introduced in Section 4 requires the in-sensor storage of the K coding tensors ($\mathbf{C} = (\mathbf{C}_k)_{k=0}^{K-1}$) that are used for compression. This means that a large $\mathbf{C}$ may introduce a significant amount of in-sensor memory overhead, making these designs for $\mathbf{C}$ less practical. In this section, we provide a quantitative analysis of this memory overhead for different coding tensor designs.

Recall that $\boldsymbol{H}$ and $\mathbf{C}$ are $N_t \times N_r \times N_c$ and $K \times M_t \times M_r \times M_c$ tensors, respectively. Let, $N = N_t \cdot N_r \cdot N_c$ be the total number of elements in the histogram tensor. Moreover, let $M = M_t \cdot M_r \cdot M_c$ the size of a single coding tensor which is also the size of the histogram block, $\boldsymbol{H}_b$ that we are compressing. For the remainder of this analysis, we assume the following:

1. We assume that all histogram blocks $\boldsymbol{H}_b$ that are compressed are non-overlapping. This means that the total number of compressive histograms that are transferred off-sensor is $B = N/M$.
2. We assume that only a single $\mathbf{C}$ is stored inside the sensor. This $\mathbf{C}$ will be shared among all SPAD pixels.
3. We assume that the elements of $\mathbf{C}$ and $\boldsymbol{H}$ are represented using the same number of bits.

Table 1 provides the expected compression ratios for off-sensor data transmission and in-sensor storage. These two compression ratios will differ due to the memory overhead incurred by compressive histograms when having to store the coding tensors $\mathbf{C}$. It is clear that a compressive histogram for a histogram block whose size equals the size of the histogram tensor (i.e., $M = N$), would actually require more in-sensor memory than the histogram tensor making this compressive histogram design impractical.

	Histogram Tensor	**Compressive Histograms**	**Compression Ratios**
Off-sensor Data Transmission	N	$B \cdot K$	$N/(B \cdot K)$
In-sensor Storage	N	$(K \cdot B) + (K \cdot M) = K \cdot (B + M)$	$N/(K \cdot (B + M))$

Table 1. **Data Transmission and In-sensor Storage Requirements.** This table shows the off-sensor data transmission and in-sensor storage requirements for a histogram tensor of size N and a set of B compressive histograms that use K coding tensors of size M for compression. The compression ratio column shows the amount of compression that can be achieved for off-sensor data transmission and in-sensor storage.

Compression Ratios for *Full* Coding Tensors: Fig. 15 shows the expected compression ratios for different histogram tensor and coding tensor sizes. As we reduce the number of compressive histograms to represent the histogram tensor, the size of the coding tensors will increase and consequently we achieve lower in-sensor compression. Since the coding tensors do not need to be transferred off-sensor, the data rate compression ratio continue to increase as we reduce the number of compressive histograms because the overall size of the compressive representation does decrease when K is fixed. Overall, a good balance between reducing in-sensor memory and data transmission seems to be achieved when using 10,000-100,000 compressive histograms to represent a histogram tensor with 1e9 element (e.g., a 1 megapixel SPAD array with 1000 bins per pixel). In this case, the size of a single coding tensor (M) should range between $10,000 - 100,000$ for $64 \leq K \leq 512$. Some of the coding tensors with $K \geq 64$ that were evaluated in this paper approximately match this size range, e.g., $M = 16,384$ for $1024 \times 4 \times 4$ or for $256 \times 8 \times 8$.

Compression Ratios for *Separable* Coding Tensors: Fig. 16 shows the expected compression ratios for different histogram tensor and coding tensor sizes for a separable coding tensor that is 16x smaller than a full coding tensor. A separable coding tensor that is $\sim$ 16x smaller is consistent with the separable coding tensors used in the main paper. For instance, a $256 \times 4 \times 4$ $\mathbf{C}_k$ is $\sim$ 16x smaller if we make its temporal and spatial dimensions separable. In this scenario, a good balance between in-sensor storage and data transmission compression is achieved when using 1,000-100,000 compressive histograms to represent a histogram tensor with 1e9 elements. In this case, the size of a single separable coding tensor should range between $625 - 62,500$ for $64 \leq K \leq 512$. Some of the separable coding tensors with $K \geq 64$ that were evaluated in this paper approximately match this size range: $M = 272$ ($256 \times 4 \times 4$), $M = 1040$ ($1024 \times 4 \times 4$).

Summary: Parameter-efficient coding tensors can reduce the in-sensor memory overhead that compressive histograms introduce. In this section, we show that the local block-based separable coding tensor designs explored in this paper are able to reduce the memory overhead for histogram tensors of size $N \geq$ 1e7. Additional lightweight $\mathbf{C}$ designs could rely on other factorization techniques such as low-rank approximations. Moreover, as shown in Suppl. Sec. S. 2, weight quantization can be an extremely effective technique in further compressing $\mathbf{C}$. Finally, $\mathbf{C}$ designs whose parameters can be computed on the fly, such as Fourier-based (Suppl. Sec. S. 2) or Gray codes [16], are a practical design when multiple $\mathbf{C}$ need to be stored across the SPAD array. Ultimately, a practical coding tensor representation will be determined by the hardware constraints of a given SPAD camera.

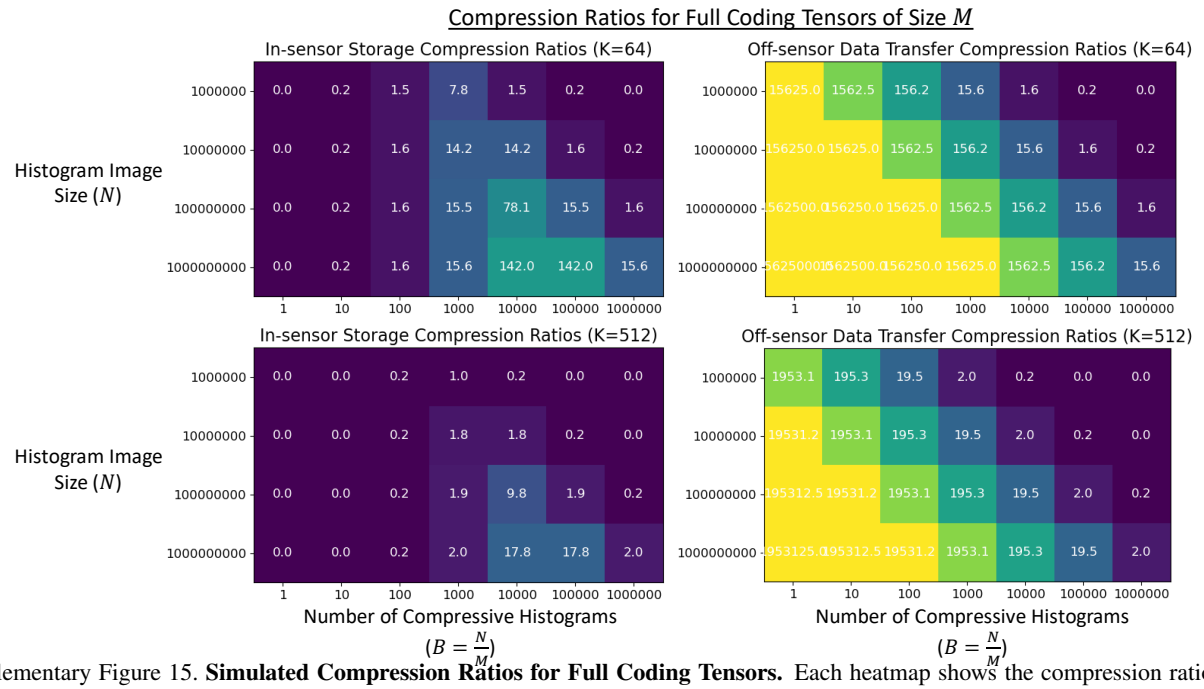

Supplementary Figure 15. **Simulated Compression Ratios for Full Coding Tensors.** Each heatmap shows the compression ratio for a fixed K for different histogram tensor sizes (B) and number of compressive histograms (B) that are used. The compression ratios for in-sensor storage (left column) and data transfer (right column) are computed using the equations in Table 1.

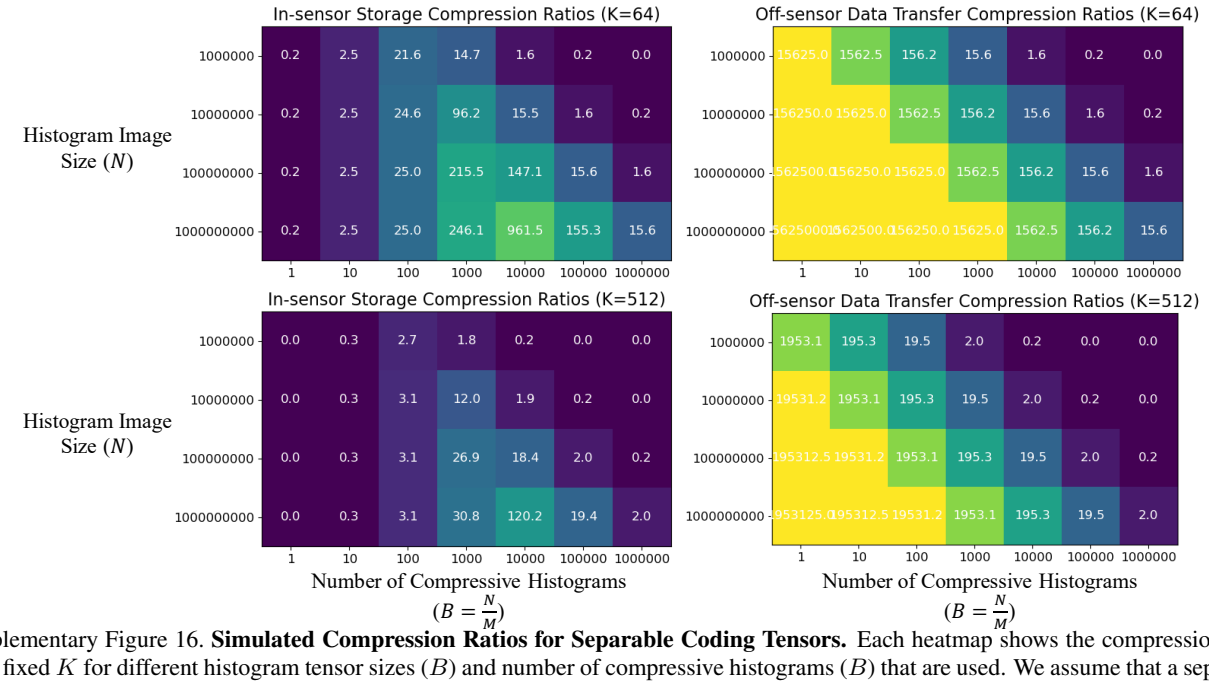

Supplementary Figure 16. **Simulated Compression Ratios for Separable Coding Tensors.** Each heatmap shows the compression ratio for a fixed K for different histogram tensor sizes (B) and number of compressive histograms (B) that are used. We assume that a separable coding tensor is 16x smaller than a full coding tensor, which is consistent with the separable coding tensors used in the paper. The compression ratios for in-sensor storage and data transfer are computed using the equations in Table 1 replacing M with $M/16$.

S. 7. Additional Coding Tensor Visualization

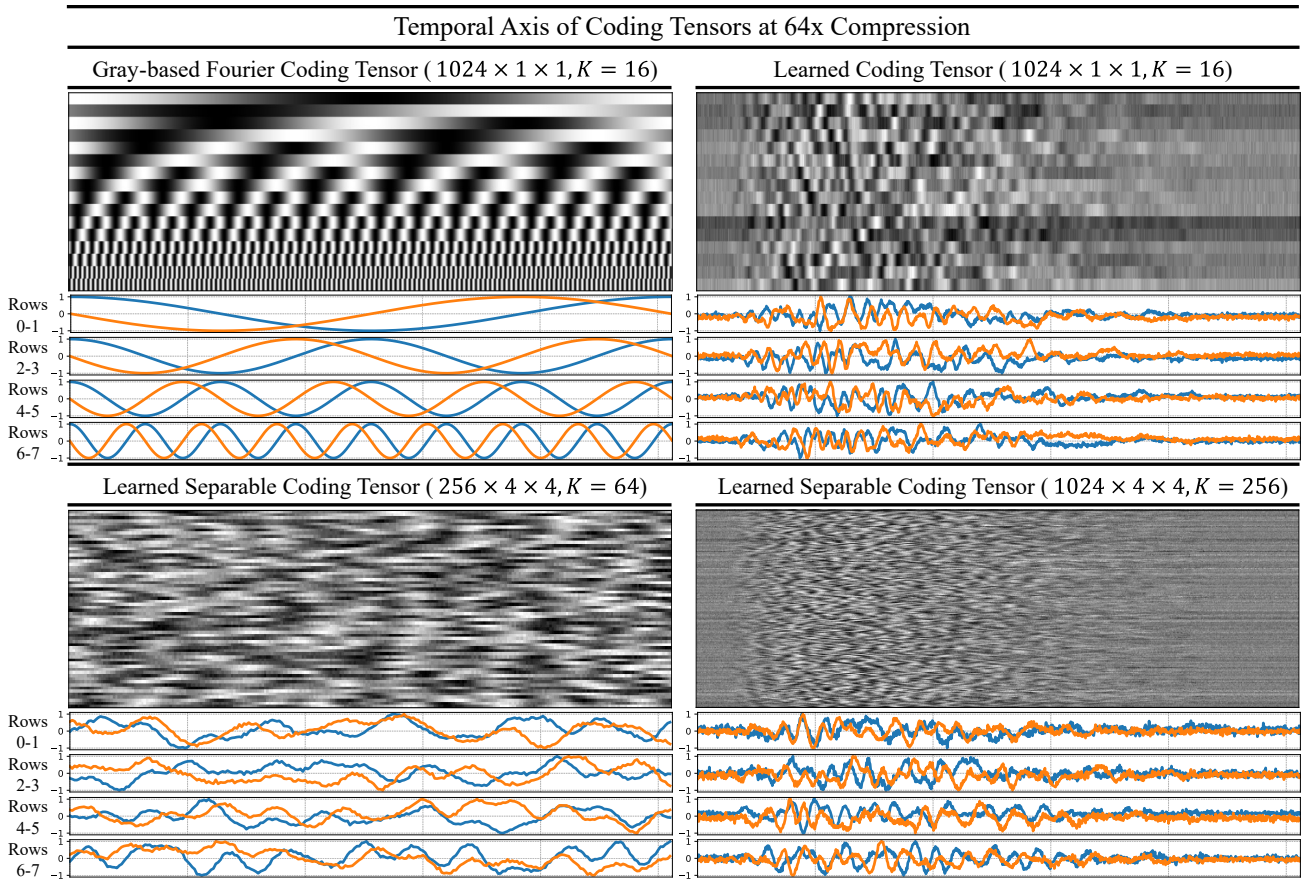

Supplementary Figure 17. **Temporal Dimension of C at 64x Compression** Visualization of the temporal dimension for different coding tensors that achieve 64x compression. The matrix visualized for coding tensors of dimension $1024 \times 1 \times 1$ (columns 1 and 2) is an 16×1024 matrix, since $K = 16$ and $M_t = 1024$. On the other hand, the matrix for the learned separable $256 \times 4 \times 4$ $\mathbf{C}_k$ is 64×256 since $K = 64$ and $M_t = 256$. Similarly, the matrix for the learned separable $1024 \times 4 \times 4$ $\mathbf{C}_k$ is a 256×1024 matrix. The functions shown below each matrix correspond to different rows of the matrix. The Gray Fourier matrix corresponds to the compressive histogram method proposed in [16].

References

[1] How multi-beam flash lidar works. https://ouster.com/blog/how-multi-beam-flash-lidar-works/. Accessed: 2022-03-07. 1

[2] The iphone 12 - lidar at your fingertips. https://www.forbes.com/sites/sabbirrangwala/2020/11/12/the-iphone-12lidar-at-your-fingertips/?sh=580b8bab3e28. Accessed: 2022-03-07. 1

[3] Supreeth Achar, Joseph R Bartels, William L Whittaker, Kiriakos N Kutulakos, and Srinivasa G Narasimhan. Epipolar time-of-flight imaging. *ACM Transactions on Graphics (TOG)*, 36(4):37, 2017. 3

[4] Andrei Ardelean. Computational imaging spad cameras. page 164, 2023. 2, 8, 4, 5

[5] Jimmy Lei Ba, Jamie Ryan Kiros, and Geoffrey E Hinton. Layer normalization. *arXiv preprint arXiv:1607.06450*, 2016. 5, 16

[6] Laurie Bose, Jianing Chen, Stephen J Carey, Piotr Dudek, and Walterio Mayol-Cuevas. A camera that cnns: Towards embedded neural networks on pixel processor arrays. In *Proceedings of the IEEE/CVF International Conference on Computer Vision*, pages 1335–1344, 2019. 2, 4

[7] Laurie Bose, Piotr Dudek, Jianing Chen, Stephen J Carey, and Walterio W Mayol-Cuevas. Fully embedding fast convolutional networks on pixel processor arrays. In *European Conference on Computer Vision*, pages 488–503. Springer, 2020. 2

[8] Samuel Burri, Claudio Bruschini, and Edoardo Charbon. Linospad: a compact linear spad camera system with 64 fpga-based tdc modules for versatile 50 ps resolution time-resolved imaging. *Instruments*, 1(1):6, 2017. 13

[9] Wenzheng Chen, Parsa Mirdehghan, Sanja Fidler, and Kiriakos N Kutulakos. Auto-tuning structured light by optical stochastic gradient descent. In *Proceedings of the IEEE/CVF Conference on Computer Vision and Pattern Recognition*, pages 5970–5980, 2020. 16

[10] Francesco Mattioli Della Rocca, Hanning Mai, Sam W Hutchings, Tarek Al Abbas, Kasper Buckbee, Andreas Tsiamis, Peter Lomax, Istvan Gyongy, Neale AW Dutton, and Robert K Henderson. A 128× 128 spad motion-triggered time-of-flight image sensor with in-pixel histogram and column-parallel vision processor. *IEEE Journal of Solid-State Circuits*, 55(7):1762–1775, 2020. 2

[11] Piotr Dudek, Thomas Richardson, Laurie Bose, Stephen Carey, Jianing Chen, Colin Greatwood, Yanan Liu, and Walterio Mayol-Cuevas. Sensor-level computer vision with pixel processor arrays for agile robots. *Science Robotics*, 7(67):eabl7755, 2022. 2

[12] Daniele Faccio, Andreas Velten, and Gordon Wetzstein. Non-line-of-sight imaging. *Nature Reviews Physics*, 2(6):318–327, 2020. 9

[13] Anant Gupta, Atul Ingle, and Mohit Gupta. Asynchronous single-photon 3d imaging. In *Proceedings of the IEEE International Conference on Computer Vision*, pages 7909–7918, 2019. 3

[14] Anant Gupta, Atul Ingle, Andreas Velten, and Mohit Gupta. Photon-flooded single-photon 3d cameras. In *Proceedings of the IEEE Conference on Computer Vision and Pattern Recognition*, pages 6770–6779, 2019. 3

[15] Felipe Gutierrez-Barragan, Huaijin Chen, Mohit Gupta, Andreas Velten, and Jinwei Gu. itof2dtof: A robust and flexible representation for data-driven time-of-flight imaging. *arXiv preprint arXiv:2103.07087*, 2021. 16

[16] Felipe Gutierrez-Barragan, Atul Ingle, Trevor Seets, Mohit Gupta, and Andreas Velten. Compressive single-photon 3d cameras. In *Proceedings of the IEEE/CVF Conference on Computer Vision and Pattern Recognition*, pages 17854–17864, 2022. 2, 3, 4, 5, 6, 9, 1, 7, 11, 13, 14, 16, 18, 20

[17] Felipe Gutierrez-Barragan, Syed Azer Reza, Andreas Velten, and Mohit Gupta. Practical coding function design for time-of-flight imaging. In *Proceedings of the IEEE Conference on Computer Vision and Pattern Recognition*, pages 1566–1574, 2019. 5, 16

[18] Istvan Gyongy, Sam W Hutchings, Abderrahim Halimi, Max Tyler, Susan Chan, Feng Zhu, Stephen McLaughlin, Robert K Henderson, and Jonathan Leach. High-speed 3d sensing via hybrid-mode imaging and guided upsampling. *Optica*, 7(10):1253–1260, 2020. 1, 2, 3

[19] Felix Heide, Steven Diamond, David B Lindell, and Gordon Wetzstein. Sub-picosecond photon-efficient 3d imaging using single-photon sensors. *Scientific reports*, 8(1):1–8, 2018. 3

[20] Andrew G Howard, Menglong Zhu, Bo Chen, Dmitry Kalenichenko, Weijun Wang, Tobias Weyand, Marco Andreetto, and Hartwig Adam. Mobilenets: Efficient convolutional neural networks for mobile vision applications. *arXiv preprint arXiv:1704.04861*, 2017. 4

[21] Sam W Hutchings, Nick Johnston, Istvan Gyongy, Tarek Al Abbas, Neale AW Dutton, Max Tyler, Susan Chan, Jonathan Leach, and Robert K Henderson. A reconfigurable 3-d-stacked spad imager with in-pixel histogramming for flash lidar or high-speed time-of-flight imaging. *IEEE Journal of Solid-State Circuits*, 54(11):2947–2956, 2019. 2

[22] Diederik P Kingma and Jimmy Ba. Adam: A method for stochastic optimization. *arXiv preprint arXiv:1412.6980*, 2014. 5, 17

[23] Oichi Kumagai, Junichi Ohmachi, Masao Matsumura, Shinichiro Yagi, Kenichi Tayu, Keitaro Amagawa, Tomohiro Matsukawa, Osamu Ozawa, Daisuke Hirono, Yasuhiro Shinozuka, et al. A 189x600 back-illuminated stacked spad direct time-of-flight depth sensor for automotive lidar systems. In *2021 IEEE International Solid-State Circuits Conference (ISSCC)*, volume 64, pages 110–112. IEEE, 2021. 2

[24] David B Lindell, Matthew O'Toole, and Gordon Wetzstein. Single-photon 3d imaging with deep sensor fusion. *ACM Trans. Graph.*, 37(4):113–1, 2018. 4, 5, 8, 1, 13, 14, 15, 16

[25] David B Lindell and Gordon Wetzstein. Three-dimensional imaging through scattering media based on confocal diffuse tomography. *Nature communications*, 11(1):1–8, 2020. 9

[26] Xiaochun Liu, Sebastian Bauer, and Andreas Velten. Phasor field diffraction based reconstruction for fast non-line-of-sight imaging systems. *Nature communications*, 11(1):1–13, 2020. 9

[27] Ashley Lyons, Francesco Tonolini, Alessandro Boccolini, Audrey Repetti, Robert Henderson, Yves Wiaux, and Daniele Faccio. Computational time-of-flight diffuse optical tomography. *Nature Photonics*, 13(8):575–579, 2019. 9

[28] Julien NP Martel, Lorenz K Mueller, Stephen J Carey, Piotr Dudek, and Gordon Wetzstein. Neural sensors: Learning pixel exposures for hdr imaging and video compressive sensing with programmable sensors. *IEEE Transactions on Pattern Analysis and Machine Intelligence*, 42(7):1642–1653, 2020. 2

[29] Parsa Mirdehghan, Wenzheng Chen, and Kiriakos N Kutulakos. Optimal structured light à la carte. In *Proceedings of the IEEE Conference on Computer Vision and Pattern Recognition*, pages 6248–6257, 2018. 5, 16

[30] Kazuhiro Morimoto, Andrei Ardelean, Ming-Lo Wu, Arin Can Ulku, Ivan Michel Antolovic, Claudio Bruschini, and Edoardo Charbon. Megapixel time-gated spad image sensor for 2d and 3d imaging applications. *Optica*, 7(4):346–354, 2020. 1

[31] K Morimoto, J Iwata, M Shinohara, H Sekine, A Abdelghafar, H Tsuchiya, Y Kuroda, K Tojima, W Endo, Y Maehashi, et al. 3.2 megapixel 3d-stacked charge focusing spad for low-light imaging and depth sensing. In *2021 IEEE International Electron Devices Meeting (IEDM)*, pages 20–2. IEEE, 2021. 1

[32] Ji Hyun Nam, Eric Brandt, Sebastian Bauer, Xiaochun Liu, Marco Renna, Alberto Tosi, Eftychios Sifakis, and Andreas Velten. Low-latency time-of-flight non-line-of-sight imaging at 5 frames per second. *Nature communications*, 12(1):1–10, 2021. 9

[33] Cindy M Nguyen, Julien NP Martel, and Gordon Wetzstein. Learning spatially varying pixel exposures for motion deblurring. *arXiv preprint arXiv:2204.07267*, 2022. 2

[34] Adam Paszke, Sam Gross, Francisco Massa, Adam Lerer, James Bradbury, Gregory Chanan, Trevor Killeen, Zeming Lin, Natalia Gimelshein, Luca Antiga, et al. Pytorch: An imperative style, high-performance deep learning library. In *Advances in neural information processing systems*, pages 8026–8037, 2019. 16

[35] Sara Pellegrini, Gerald S Buller, Jason M Smith, Andrew M Wallace, and Sergio Cova. Laser-based distance measurement using picosecond resolution time-correlated single-photon counting. *Measurement Science and Technology*, 11(6):712, 2000. 1

[36] Jiayong Peng, Zhiwei Xiong, Xin Huang, Zheng-Ping Li, Dong Liu, and Feihu Xu. Photon-efficient 3d imaging with a non-local neural network. In *European Conference on Computer Vision*, pages 225–241. Springer, 2020. 2, 4, 5, 6, 16

[37] Valentin Poisson, William Guicquero, Gilles Sicard, et al. Luminance-depth reconstruction from compressed time-of-flight histograms. *IEEE Transactions on Computational Imaging*, 8:148–161, 2022. 2

[38] Kayvan Samimi, Danielle E Desa, Wei Lin, Kurt Weiss, Joe Li, Jan Huisken, Veronika Miskolci, Anna Huttenlocher, Jenu V Chacko, Andreas Velten, et al. Light sheet autofluorescence lifetime imaging with a single photon avalanche diode array. *bioRxiv*, pages 2023–02, 2023. 9

[39] Daniel Scharstein and Chris Pal. Learning conditional random fields for stereo. In *2007 IEEE Conference on Computer Vision and Pattern Recognition*, pages 1–8. IEEE, 2007. 5

[40] Michael P. Sheehan, Julián Tachella, and Mike E. Davies. A sketching framework for reduced data transfer in photon counting lidar. *IEEE Transactions on Computational Imaging*, 7:989–1004, 2021. 2, 3, 4, 6, 9, 11, 13, 14, 16

[41] Michael P Sheehan, Julián Tachella, and Mike E Davies. Surface detection for sketched single photon lidar. *arXiv preprint arXiv:2105.06920*, 2021. 2

[42] Nathan Silberman, Derek Hoiem, Pushmeet Kohli, and Rob Fergus. Indoor segmentation and support inference from rgbd images. In *European conference on computer vision*, pages 746–760. Springer, 2012. 5

[43] Haley M So, Julien NP Martel, Piotr Dudek, and Gordon Wetzstein. Mantissacam: Learning snapshot high-dynamic-range imaging with perceptually-based in-pixel irradiance encoding. *arXiv preprint arXiv:2112.05221*, 2021. 2

[44] Zhanghao Sun, David B Lindell, Olav Solgaard, and Gordon Wetzstein. Spadnet: deep rgb-spad sensor fusion assisted by monocular depth estimation. *Optics express*, 28(10):14948–14962, 2020. 5, 16

[45] Julián Tachella, Michael P Sheehan, and Mike E Davies. Sketched rt3d: How to reconstruct billions of photons per second. In *ICASSP 2022-2022 IEEE International Conference on Acoustics, Speech and Signal Processing (ICASSP)*, pages 1566–1570. IEEE, 2022. 2

[46] Arin Can Ulku, Claudio Bruschini, Ivan Michel Antolović, Yung Kuo, Rinat Ankri, Shimon Weiss, Xavier Michalet, and Edoardo Charbon. A 512× 512 spad image sensor with integrated gating for widefield flim. *IEEE Journal of Selected Topics in Quantum Electronics*, 25(1):1–12, 2018. 8, 5

[47] Edwin Vargas, Julien NP Martel, Gordon Wetzstein, and Henry Arguello. Time-multiplexed coded aperture imaging: Learned coded aperture and pixel exposures for compressive imaging systems. In *Proceedings of the IEEE/CVF International Conference on Computer Vision*, pages 2692–2702, 2021. 2

[48] Augusto Ronchini Ximenes, Preethi Padmanabhan, Myung-Jae Lee, Yuichiro Yamashita, Dun-Nian Yaung, and Edoardo Charbon. A modular, direct time-of-flight depth sensor in 45/65-nm 3-d-stacked cmos technology. *IEEE Journal of Solid-State Circuits*, 54(11):3203–3214, 2019. 4

[49] Chao Zhang, Ning Zhang, Zhijie Ma, Letian Wang, Yu Qin, Jieyang Jia, and Kai Zang. A 240× 160 3d-stacked spad dtof image sensor with rolling shutter and in-pixel histogram for mobile devices. *IEEE Open Journal of the Solid-State Circuits Society*, 2:3–11, 2021. 4

[50] Yongyi Zhao, Ankit Raghuram, Hyun Kim, Andreas Hielscher, Jacob T Robinson, and Ashok Narayanan Veeraraghavan. High resolution, deep imaging using confocal time-of-flight diffuse optical tomography. *IEEE Transactions on Pattern Analysis and Machine Intelligence*, 2021. 9